Validity criteria for the small slope approximation for backscattering of sound from rough surfaces with a power-law roughness spectrum

Derek R. Olson[a]
Oceanography Department, Naval Postgraduate School, Monterey, CA 93943

(Dated: 7 August 2026)

The small slope approximation is a commonly-used model for scattering of waves from rough surfaces. Its limitations are currently unknown for a power-law roughness spectral density, used to model natural terrain and seafloor roughness. This work compares the small slope approximation to the boundary element method, a numerical solution of the Helmholtz boundary integral equations governing acoustic scattering. These comparisons were used to find the validity limits as a function of dimensionless root mean square height, kh, and root mean square slope, s, where k is the wavenumber. The two lowest terms in the small slope series were used, and both the Dirichlet and fluid-fluid boundary conditions were examined. Both kh and s are found to be important parameters for the validity of the small slope approximation. Different spectral exponents have similar maximum valid kh. The maximum s is almost constant as a function of the power law outer scale, but varies as a function of the spectral exponent. Comparisons with other scattering models are discussed, and aspects of scattering from very large roughness are explored.

[https://doi.org(DOI number)]

[XYZ] Pages: 1–19

I. INTRODUCTION

Acoustic scattering from the seafloor is a major source of interference for undersea detection systems[1–3]. It also contains a rich set of information regarding the composition and roughness properties of the seafloor, meaning that it can be used for remote sensing[4,5]. Both target detection performance prediction and remote sensing require accurate models relating observable acoustic quantities to seafloor geoacoustic and roughness properties[2,4]. One of the most common acoustic observables is the scattering cross-section per unit area per unit solid angle of the seafloor[6], which will be described as the "scattering cross-section" in this work.

There are three widely-used models for scattering from natural roughness: small-roughness perturbation theory (PT)[7–10], the Kirchhoff approximation (KA)[11–13] (also known as the tangent plane approximation), and the small-slope approximation (SSA)[14–17]. The composite roughness approximation has also been used for remote sensing[4,12,18], but its use has largely been superseded by the SSA[6 19 20]. PT is commonly understood to be accurate for small grazing angles, and the KA to be accurate for large backscattering grazing angles[6,10,21](more generally, near the specular direction). These models, including the SSA, have also been used extensively in the problem of electromagnetic wave scattering and emission from the ocean surface[22–31], and natural terrain[32].

The SSA is the current state of the art for seafloor scattering models given its applicability at both small and large grazing angles[14,16,17,19,33], but its validity in general has not been widely studied. Determination of the limits of validity of scattering models has been an active area of research since the 1980s. Previous work by Thorsos[21] has studied the validity of the KA for a Gaussian roughness spectrum, PT for Gaussian roughness[10], and both PT and KA for Pierson-Moskowitz ocean surface roughness[34]. Later work by Broschat and Thorsos[35] investigated the validity of the SSA for Gaussian roughness. Wang and Broschat studied the validity of the SSA using a Pierson-Moskowitz spectrum[36]. All of these works used Dirichlet boundary conditions with 1-D rough interfaces in a 2-D wave propagation medium, and studied bistatic geometry for a few incident angles. The Gaussian roughness spectrum model has a single horizontal scale, the characteristic or correlation length, L_G, whereas the Pierson-Moskowitz spectrum is multiscale at large wave-numbers (behaving like a power law with exponent of three for one-dimensional (1D) roughness), and contains a peak at non-zero horizontal wave-number, K_p.

Seafloor and natural terrain tend to have power law roughness spectra over a wide variety of spatial scales, and have a power-law exponent between 1 and 3 for measured 1D roughness profiles[37–39]. To date, there has been no numerical study to determine the roughness properties and angles for which the SSA is accurate for power-law surfaces (other than the Pierson-Moskowitz spectrum[36]), and no work for the fluid-fluid (also known as transmission[40]) boundary conditions. Prior work used

[a]derek.olson@nps.edu

bistatic geometry, but many of the remote sensing systems currently in use, such as multibeam sonar, sidescan sonar, synthetic aperture sonar, and radar scatterometers, use a monostatic, or backscattering, geometry.

This work performs an examination of the validity of the SSA using backscattering geometry for power-law spectra by comparing the two lowest-order terms of the SSA T-matrix with the results of the numerical solution of the Helmholtz-Kirchhoff integral equation (IE). The lowest-order SSA is most commonly used for modeling seafloor scattering[19,33,41–44], but the next higher term also has potential for use in remote sensing for rougher surfaces or higher frequencies and is studied here as well. A 1D rough surface is employed here. While unrealistic, the 1D model enables the large number of simulations required to be run with modest resource use on a high performance computing system, whereas two-dimentional roughness would be prohibitive without fast approximations, such as the fast multipole method[45,46]. Both Dirichlet and fluid-fluid boundary conditions are studied in this work. Two sets of fluid parameters are used, one approximating a sand seafloor, and another approximating mud, to provide situations with and without a critical angle. A small number of comparison between the SSA and the PT and KA are given to show situations in which they agree with the SSA.

This work is organized as follows. A description of the environment is given in Sec. II. An overview of the small slope approximation and numerical methods are given in Sec. III. The parameters of the numerical experiments and the validity criterion are detailed in Sec IV. Results are given in Sec. V, and discussed in Sec. VI. Conclusions are given in Sec. VII.

II. ENVIRONMENT

The acoustic environment consists of two half spaces separated by a rough boundary. Although sub-bottom structure is often present in seafloor and has an impact on the scattering cross-section[47–52], attention is restricted in this work to a single rough interface for simplicity. A diagram of the environment is shown in Fig. 1. The upper half space has a sound speed c_0 and density ρ_0 and is assumed to have no dissipation. The lower medium has a phase speed c_1 and density ρ_1. Dissipation in the lower medium is quantified by the ratio of the imaginary to real part of the acoustic wave-number, δ_1. The complex sound speed is $\tilde{c}_1 = c_1/(1 + i\delta_1)$, where $i = \sqrt{-1}$. Sound speed and density are analyzed here in terms of the dimensionless ratios $a_c = c_1/c_0$ and $a_\rho = \rho_1/\rho_0$. Dirichlet boundary conditions can be obtained by taking the limit as both of the dimensionless ratios tend to zero. The acoustic wave-number in the water is $k_0 = \omega/c_0$, and $k_1 = \omega/\tilde{c}_1$ is the wave-number in the lower half-space. The shorthand $k = k_0$ will be used in nondimensional quantities such as kh and kL. The wavelength in water is $\lambda = 2\pi/k$.

The rough surface is denoted by $z = f(x)$. This random process is characterized by its power spectral density, $W(k_x)$ as a function of horizontal wave-number k_x. The power spectrum is defined as

$$W(k_x) = \frac{1}{2\pi} \int \mathrm{d}x B_{ff}(x) e^{-ik_x x} \tag{1}$$

where

$$B_{ff}(x) = E[f(x_1)f(x + x_1)] \tag{2}$$

is the roughness autocovariance function, $E[\cdot]$ is the formal expectation operator, and x_1 is a dummy variable to show that the rough interface is assumed to be wide-sense statistically homogeneous (the spatial equivalent of wide-sense stationary[53,54]). The Fourier transform of the $f(x)$ is denoted as $F(k_x)$, with the power spectrum defined in terms of F by

$$W(k_x)\delta(k_x - k'_x) = E\left[F(k_x)F^*(k'_x)\right]. \tag{3}$$

The delta function is a consequence of the wide-sense homogeneous property and indicates that disparate wave-numbers are statistically independent[55].

The model used here for the power spectral density is a truncated power law given by[51]

$$W(k_x) = \frac{w}{|k_x|^\gamma} \tag{4}$$

for $k_L \le |k_x| \le k_u$, and zero otherwise. In this model, w is the spectral strength, and γ is the spectral exponent. The wave-number lower limit is $k_L = 2\pi/L$, where L is the outer scale, and the upper limit is $k_u = 2\pi/\ell$ where ℓ is the inner scale. Limits are introduced because a pure power-law model can have infinite rms height and rms slope, and because an abrupt truncation is convenient when dealing with discretized rough surfaces in the numerical simulations.

With this form, the dimensionless mean square height of this spectrum is[51]

$$(kh)^2 = \frac{2k^{3-\gamma}w}{\gamma - 1}\left(\left(\frac{2\pi}{kL}\right)^{1-\gamma} - \left(\frac{2\pi}{k\ell}\right)^{1-\gamma}\right), \tag{5}$$

and the mean square slope is

$$s^2 = \frac{2k^{3-\gamma}w}{3 - \gamma}\left(\left(\frac{2\pi}{k\ell}\right)^{3-\gamma} - \left(\frac{2\pi}{kL}\right)^{3-\gamma}\right). \tag{6}$$

Taking the limit of $\gamma \to 1$, the dimensionless mean square height is

$$\lim_{\gamma\to 1}(kh)^2 = 2k^2 w \ln\left(\frac{L}{\ell}\right). \tag{7}$$

In the limit of $\gamma \to 3$, the mean square slope is

$$\lim_{\gamma\to 3} s^2 = 2k^2 w \ln\left(\frac{L}{\ell}\right). \tag{8}$$

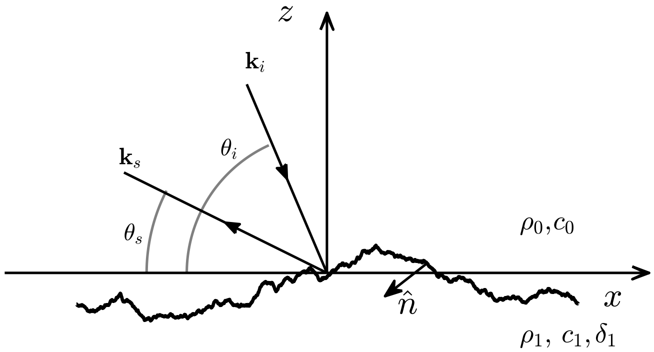

FIG. 1. A diagram depicting the scattering geometry. The incident and scattered wave vectors are shown, along with the definition of the incident and scattered grazing angles, surface normal vector, and indication of the geoacoustic properties of each medium.

The incident field in this work is an approximation of a plane wave with wave vector $\vec{k}_i = (k_{ix}, k_{iz}) = (k_{ix}, -\kappa_{iz})$ and direction

$$\hat{k}_i = \frac{\vec{k}_i}{k} = (\cos(\theta), -\sin(\theta))\,, \tag{9}$$

where θ is the backscattering grazing angle. The scattered field is measured at a point in the far field, where the field can be assumed to have a single direction,

$$\hat{k}_s = \frac{\vec{k}_s}{k_0} = (-\cos(\theta), \sin(\theta)) \tag{10}$$

where the same angular argument (with different signs for the component) is used because backscattering geometry is used in this work. The scattered wave vector is defined as $\vec{k}_s = k\hat{k}_s = (k_{sx}, k_{sz})$. The unit normal to the surface is $\hat{n} = (df/dx, -1)/\sqrt{1 + (df/dx)^2}$. The incident and scattered wave vectors, rough surface, normal vector and coordinate axes are shown in Fig. 1. Note that the variables θ_i and θ_s are shown to distinguish the incident and scattered wave vectors for illustration purposes.

The incident pressure used here follows a modified Gaussian beam developed by Thorsos[21] to mitigate the effects of truncation of the rough interface. It is defined as

$$p_i(\mathbf{r}) = p_0 e^{\mathrm{i}\mathbf{k}_i\cdot\mathbf{r}(1+w(\mathbf{r})-(x-z\cot\theta_i)^2/g^2)} \tag{11}$$

where

$$w(\mathbf{r}) = \frac{2\left(x - z\cot\theta_i\right)^2/g^2 - 1}{\left(kg\sin\theta_i\right)^2}\,, \tag{12}$$

and the incident field is given units by the constant p_0.

III. METHODS

A. The scattering cross-section and the T matrix

The acoustic quantity examined in this work is the scattering cross-section per unit length per unit angle, $\sigma(k_{sx}, k_{ix})$. One method of calculating it uses the transition, or T-matrix, T, which is a complex-valued transfer function between incoming and outgoing plane-wave amplitudes[6,10,14]. The full (2×2) T-matrix for fluid-fluid rough interface scattering characterizes the transfer function between incident plane waves from both above and below a rough interface, and scattered plane waves above and below the rough surface[56]. In this work, only the T-matrix element for an incident wave from the upper medium to a scattered wave in the upper medium is used, and the symbol T is used to stand in for this scalar.

The scattering cross-section for 2D geometry is defined as[10,35]

$$\sigma(k_{sx}, k_{ix}) = \frac{k_{sz}^2}{k} C(k_{sx}, k_{ix})\,, \tag{13}$$

where $C(k_{sx}, k_{ix})$ is the second moment of the T-matrix[10],

$$C(k_{sx}, k_{ix})\delta(k_{ix} - k'_{ix}) = E[T_I(k_{sx}, k_{ix})T_I^*(k_{sx}, k'_{ix})]\,, \tag{14}$$

The incoherent T-matrix is $T_I = T - \bar{T}$ and the mean T-matrix is

$$\bar{T}(k_{sx}, k_{ix}) = E[T(k_{sx}, k_{ix})]\,. \tag{15}$$

The T-matrix characterizes the relationship between the incoming plane-wave spectrum, $A_i(k_x)$ and the scattered plane-wave spectrum, $A_s(k_x)$. Mathematically, they are related by

$$A_s(k_{sx}) = \int \mathrm{d}k_x T(k_{sx}, k_x) A_i(k_x)\,. \tag{16}$$

The formal averages used above are smooth functions. The numerical results from the integral equation method (described below) use a finite ensemble of synthetic rough surfaces, and therefore are subject to fluctuations due to the finite ensemble. In order to compare the numerical results to the SSA in the closest way possible, we compute the acoustic models using the same rough surface realizations and calculate finite ensemble means. This same method of comparison was used by Wang and Broschat[36] and Berman[16]. In the acoustic models shown below, the rough surface will always be explicitly included either through $f(x)$ or its wave-number representation $F(k_x)$.

B. Acoustic Models

The SSA is a systematic expansion of the T-matrix whose terms are characterized by increasing powers of generalized slope[57]. The SSA as developed by Voronovich[14] starts with a form of the T-matrix that correctly changes phase based on vertical and horizontal translations of a rough surface. This form is

$$T(k_{sx}, k_{ix}) = \frac{1}{2\pi}\frac{1}{2k_{sz}} \int \mathrm{d}x e^{i\nu_x x - i\nu_z f(x)} \Phi(k_{sx}, k_{ix}, x, f(x)) \tag{17}$$

where Φ is function of incident and scattered horizontal wave-number, position, and the rough interface height. Additionally, $\nu_z = \kappa_{iz} + k_{sz}$, and $\nu_x = k_{ix} - k_{sx}$. Voronovich suggested a series for Φ of the form

$$\begin{aligned}\Phi(k_{sx}, k_{ix}, x, f) =& \Phi_0(k_{sx}, k_{ix}) + \\ & \int \mathrm{d}k_{1x} e^{ik_{1x}x} F(k_{1x}) \Phi_1(k_{sx}, k_{ix}, k_{1x}) \\ & + \dots\end{aligned} \tag{18}$$

The new variables $\Phi_0(k_{sx}, k_{ix})$ and $\Phi_1(k_{sx}, k_{ix}, k_{1x})$ are independent of x and $f(x)$ and therefore can be found by expanding Eqs. (17) and (18) in a Taylor series in $kf(x)$. This expansion is then compared to the small roughness perturbation series for T (given in the Appendix). The first two terms of the resulting SSA series are

$$T_0^{SSA} = \frac{1}{2\pi}\frac{i}{\nu_z} A_1(k_{sx}, k_{ix}) \int \mathrm{d}x e^{i\nu_x x - i\nu_z f(x)} \tag{19}$$

$$\begin{aligned}T_1^{SSA} =& \frac{1}{2\pi}\frac{i}{2\nu_z} \int \mathrm{d}x e^{i\nu_x x - i\nu_z f(x)} \\ & \times \int \mathrm{d}k_{1x} e^{ik_{1x}x} F(k_{1x}) \left(\tilde{A}_2 + i\nu_z A_1\right)\end{aligned} \tag{20}$$

The parameters A_1 and $\tilde{A}_2$ are the coefficients of the second and third terms in the perturbation series (whose arguments are suppressed here for brevity), and the tilde symbol indicates that it has been symmetrized (using the same method as Berman[16]). For fluid-fluid boundary conditions, formulae and the method of calculating A_1 and $\tilde{A}_2$ are given in the appendix. Note that the symbol A_{ww} used by Jackson[6,43] is $A_1 k_{sz}/k^2$ in the notation of this work.

For Dirichlet boundary conditions, these coefficients have been presented in the existing literature and are given by[10,16,17]

$$A_1^{(D)} = 2i\kappa_{iz} \tag{21}$$

$$\tilde{A}_2^{(D)} = 2\kappa_{iz} k \left(\beta_0(k_{ix} + k_{1x}) + \beta_0(k_{sx} - k_{1x})\right) \tag{22}$$

where $\beta_\alpha(k_x) = \sqrt{1 - k_x^2/k_\alpha^2}$ is the sine of the grazing angle corresponding to horizontal wave-number k_x in medium α. The index α can take on values of either 0 or 1 in this work.

The scattering cross-section using only T_0^{SSA} is denoted SSA(2) because it is of second order in slope. Following Broschat and Thorsos[35] and Yang and Broschat[17], we use SSA(4) to refer to the scattering cross-section using the sum of T_0^{SSA} and T_1^{SSA}. This term does not include all terms of fourth order in slope because it neglects the cross term $T_0^{SSA}(T_2^{SSA})^*$.

The zeroth-order T matrix is calculated using the rectangle rule to approximate the integral over x, which is convenient for the discretized roughness realizations used here. The first-order T-matrix is calculated using an inverse fast Fourier transform for the integral over k_{1x}, and the rectangle rule for the integral over x.

The incident field used in the numerical simulations is a tapered plane wave (discussed in Sec. III C). Therefore, the approximate plane wave was also used to compute the model results. This modification can be performed by using plane wave synthesis, and appropriately weighting the amplitude of each horizontal wave-number component. Practically, we have found that an approximation by multiplying the x integrand in Eqs. (19) and (20) by the factor $\exp(-x^2/g^2) 2^{1/2} \pi^{1/4} (g/\xi_0)^{-1/2}$ provides excellent agreement with the plane-wave synthesis method for the angles studied here. The constant ξ_0 is a unit quantity having dimensions of length. It is included to keep the preserve the units of the T matrix when using the taper. Using this factor within the integrand is equivalent to using an incident plane wave spectrum, A_i, and making the substitution

$$E[TT^*] \rightarrow \frac{E[A_s A_s^*]}{\int \mathrm{d}|A_i(k_x)|^2 k_x} \tag{23}$$

C. Numerical Methods

This section details the numerical solution to the Helmholtz integral equation[58] used as the reference solution in this work. The integral equations can be cast in terms of integral operators[59,60], which are defined by

$$\mathbb{V}_n(\phi(\mathbf{r}_1)) = \int_\Gamma G_n(\mathbf{r}_1, \mathbf{r}_2) \phi(\mathbf{r}_2) \mathrm{d}S_2 \tag{24}$$

$$\mathbb{K}_n(\phi(\mathbf{r}_1)) = \int_\Gamma \frac{\partial G_n(\mathbf{r}_1, \mathbf{r}_2)}{\partial n_2} \phi(\mathbf{r}_2) \mathrm{d}S_2 \tag{25}$$

where the 2D Green function for medium n is

$$G_n(\mathbf{r}_1, \mathbf{r}_2) = \frac{i}{4} H_0^{(1)}(k_n |\mathbf{r}_2 - \mathbf{r}_1|). \tag{26}$$

The differential arc length is dS and the subscript denotes which spatial variable of the Green function it corresponds to. In these definitions, $\mathbf{r}_1$ is a collocation point, $\mathbf{r}_2$ is an integration dummy variable, and ϕ is a test function that is the argument of the integral operator. The normal derivative $\partial/\partial n_m$ is defined as $\hat{n}_m \cdot \nabla_m$. These integral operators can be used to define integral equations for Dirichlet and transmission problems.

The integral equation for Dirichlet boundary conditions is[21]

$$\mathbb{V}_0 \frac{\partial p(\mathbf{r}_1)}{\partial n_1} = p_i(\mathbf{r}_1)\,, \tag{27}$$

where p_i is the incident pressure. Transmission (or fluid-fluid) boundary conditions are captured in the following coupled integral equations specified on the rough surface[40,60]

$$\left(\frac{1}{2}\mathbb{I} - \mathbb{K}_0\right) p(\mathbf{r}_1) + \mathbb{V}_0 \frac{\partial p(\mathbf{r}_1)}{\partial n_1} = p_i(\mathbf{r}_1) \tag{28}$$

$$\left(\frac{1}{2}\mathbb{I} + \mathbb{K}_1\right) p(\mathbf{r}_1) - a_\rho \mathbb{V}_1 \frac{\partial p(\mathbf{r}_1)}{\partial n_1} = 0\,, \tag{29}$$

where $\mathbb{I}$ is the identity operator. Once the solutions to these integral equations are found, the quantities at the surface can be used to calculate the scattered pressure, p_s at a far field point $\mathbf{r}_f$ using

$$p_s(\mathbf{r}_f) = -\mathbb{V}_0 \frac{\partial p(\mathbf{r}_1)}{\partial n_1}\,, \tag{30}$$

for Dirichlet boundary conditions, and

$$p_s(\mathbf{r}_f) = \mathbb{K}_0 p(\mathbf{r}_1) - \mathbb{V}_0 \frac{\partial p(\mathbf{r}_1)}{\partial n_1}\,, \tag{31}$$

for transmission boundary conditions.

The integral equations are discretized using the boundary element method (BEM), which uses a finite element approximation to the boundary integrals[21,61]. Previous work has also used the finite element problem for discretizing the acoustic domain, rather than the interface[62]. The integral operators were discretized using linear piece-wise functions to represent the acoustic variables at the interface and a piece-wise cubic Hermite polynomial approximation[63] to the rough interface itself, similarly to Ref. 51. The coupled integral equations in Eqs. (28) and (29) are solved by putting each discretized integral operator into a block matrix, and using LU factorization. Green's functions in the lower half space have complex wave-number, and the Amos library[64] was used to compute the Hankel functions of complex argument. The integral equation was implemented in the C programming language[65], and the zbessel library (https://github.com/jpcima/zbessel) was used to translate between the Amos Fortran library and C.

Using an ensemble of scattered pressures calculated at a distance R from the center of the rough surface, we can estimate the scattering cross-section using

$$\sigma_F = \frac{R}{L_{eff}} \frac{E[|p_s - \bar{p}_s|^2]}{|p_0|^2} \tag{32}$$

where $\bar{p}_s = E[p_s]$ is the ensemble mean of the scattered pressure, L_{eff} is the effective ensonified width of the tapered plane wave, defined by[60]

$$L_{eff} = g\sqrt{\pi/2}\left(1 - \frac{1 + 2\cot^2\theta_i}{2(kg\sin\theta_i)^2}\right)\,. \tag{33}$$

IV. NUMERICAL EXPERIMENTS AND VALIDITY CRITERION

The simulations are analyzed using nondimensional parameters that can be compared across different frequencies. The two primary parameters that will be examined are kh and kL. These have different relationships with each other depending on the value of the spectral exponent, γ, as seen from Eqs. (5) and (6). Values of γ examined were between 1 and 3 and sampled at an interval of 0.5. The values of kL examined here are $2\pi\{10, 25, 40, 55, 70, 85, 100, 150, 200\}$. The inner scale, ℓ was set to $\lambda/8$. Values of w were chosen to span regions of large and small kh and s. The upper and lower limits are shown in Table I, and used 21 logarithmically-spaced values in between. For each value of γ, the ratio between the upper and lower limit of w was 10^4.

TABLE I. Values of the spectral strength, w shown as a function of the spectral exponent, γ. Value for γ is shown in parentheses. The unit of w is $m^{3-\gamma}$. Each value of w is used for all the values of kL. Therefore, for each γ, 189 values of h and s are tested.

	$w(1.0)$	$w(1.5)$	$w(2.0)$	$w(2.5)$	$w(3.0)$
Upper Lim.	1.00e-05	1.00e-04	1.00e-03	1.00e-02	5.00e-01
Lower Lim.	1.00e-09	1.00e-08	1.00e-07	1.00e-06	5.00e-05

An error criterion of 1 dB was used in this work, which is the criterion suggested by Thorsos[10,21,34,35], and corresponds to about 25% relative error in intensity. The maximum value of the parameters, h and s, that satisfies the validity criterion is expressed by $h_{\max}$ and $s_{\max}$ respectively. The reported value of $h_{\max}$ is calculated as the greatest lower-bound of h for the valid values of w. A particular parameter combination is said to be invalid over a particular interval of backscattering angles if any of the scattering strength estimates from the integral equation differ by more than 1 dB than the model estimates. We report $kh_{\max}$ and $s_{\max}$ for three different collections of angles: all valid backscattering angles (between 10 and 90 degrees grazing angle), low grazing angles (between 10 and 40 degrees), and high grazing angles (between 70 and 90 degrees). The scattered field is sampled at 1 degree increments in this work, so the different angular regions contain 81, 31, and 21 individual angles respectively.

Determining $h_{\max}$ for a single grazing angle is a multiple hypothesis test (among different values of w). Determining $h_{\max}$ for an angular region expands the multiple comparisons test to a set of angles and a set of spectral strengths. The use of multiple comparisons increases the chances of type I and type II statistical errors[66], and the error rate increases as more comparisons are made, when compared with the test for a single angle or a single value of w. Therefore, the validity regions shown here are rather conservative, and complicated by including different numbers of grazing angles in the multiple comparison problem.

Rough surfaces were generated by starting with the square root of the sampled power spectral density, multiplying it by independent complex Gaussian random samples, enforcing the correct symmetry for real-valued rough surfaces, and then performing Fourier synthesis, similar to the process used in previous work[21,51]. The surfaces used a sampling interval of $\delta x = \lambda/14$. The incident field beam width parameter, g, was set to 100 λ for simulations where L/λ was 100 or less, and set to 200 λ for the two largest values of L/λ. The effective length, L_{eff} is larger than g by a factor of about 25%,

TABLE II. Rough interface and incident field parameters.

Parameter	Value
L_{tot}/g	4.5
g/λ	100 or 200
$\Delta x/\lambda$	1/14
N_E	100
N_{tot}	6300 or 12600

TABLE III. Geoacoustic parameters used in simulations.

Seafloor type	a_c	δ_1	a_ρ
Sand	1.1733	1.0×10^{-2}	1.845
Mud	0.982	4.5×10^{-3}	1.546

so the outer scale of the power law is captured. The total surface length, L_{tot} was set to $4.5g$ so that the incident field taper decreased to less than 1/100th of the peak at the edges. The surfaces had a total number of points of $N_{tot} = 6300$ or 12600, depending on the value of L/λ. The Monte Carlo simulations used $N_E = 100$ rough surfaces. Assuming an exponential distribution (which suitably characterized the scattered intensity), this corresponds to an uncertainty of about 10% compared with the mean intensity, which is about 0.41 dB.

Boundary conditions investigated included Dirichlet and the fluid-fluid transmission problem. Two parameter sets for the fluid-fluid boundary were used. One parameter set had a sound speed ratio greater than one and approximated medium sand. The other parameter set had a sound speed ratio less than one, smaller attenuation coefficient, and approximated mud or clay. Both density ratios were greater than one. Specific values for the fluid parameters can be found in Table III.

V. RESULTS

In this section, results of the numerical simulations are presented. First, a few cases of scattering strength are presented in which the validity criterion is not satisfied. Both SSA(2) and SSA(4) are compared with the integral equation result. Second, the validity criteria, $kh_{\max}$ and $s_{\max}$ for several boundary conditions are shown for both SSA(2) and SSA(4).

A. Examples model errors

Comparison of the scattering strength between the IE method and SSA(2) and SSA(4) are shown in this subsection. These comparisons focus on situations in which these models exceed the 1 dB threshold. Somewhat exaggerated model errors are presented here to give intuition on cases where models do not provide a good fit. Focus is placed on the trends in grazing angle.

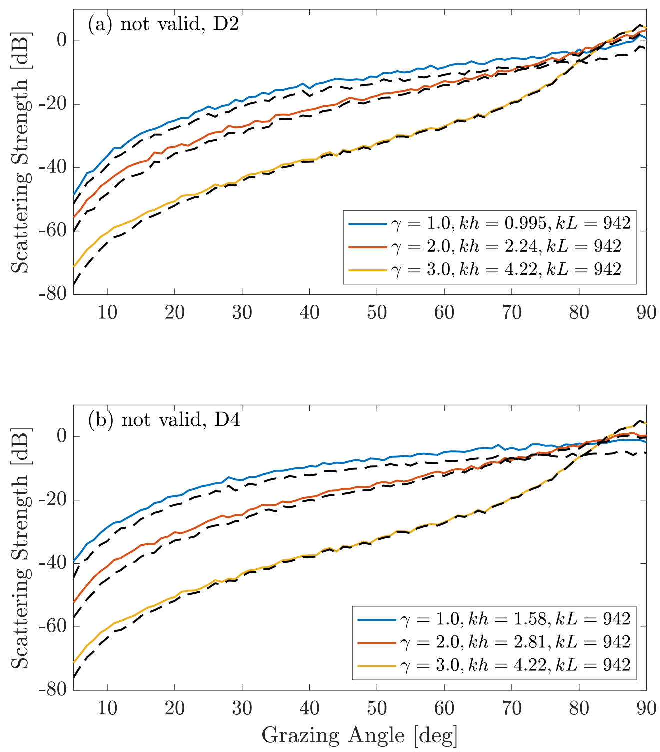

FIG. 2. Comparison between integral equation and small slope approximation (both SSA(2) and SSA(4)) using Dirichlet boundary conditions for parameter combinations that are beyond the 1 dB validity criterion. Part (a) shows SSA(2), and part (b) shows SSA(4). Three values of γ are shown by different color lines shown in the legend. Solid lines show the integral equation result, and dashed lines represent model results.

In Fig. 2, examples of model-IE comparisons are given for the Dirichlet boundary condition for parameters where SSA(2) and SSA(4) are not valid (in parts (a) and (b) respectively). Integral equation results are given by the solid lines of different colors (indicated in the legend), and the model curves are shown as black dashed lines. The spectral strength for each plot is 8 dB larger than the spectral strength that just satisfies the 1 dB validity criterion (a multiplicative factor of about 6.3 for w, and 2.5 for kh). Three values of the spectral exponent are plotted, (1.0, 2.0 and 3.0), with the colors indicated in the legend. For both SSA(2) and SSA(4) using Dirichlet boundary conditions, the integral equation exceeds the model whenever they do not agree (i.e. the model underestimates the scattering strength). For large values of γ, the error appears predominantly at low grazing angles, and is absent for larger grazing angles. For small values of γ, the error is largest near the specular direction, but scattering strength is underestimated at all grazing angles. For the intermediate case of $\gamma = 2$ (the red curves), the model is less accurate at small grazing angles than near the specular direction, but the errors begin to appear at larger grazing angles than for $\gamma = 3$.

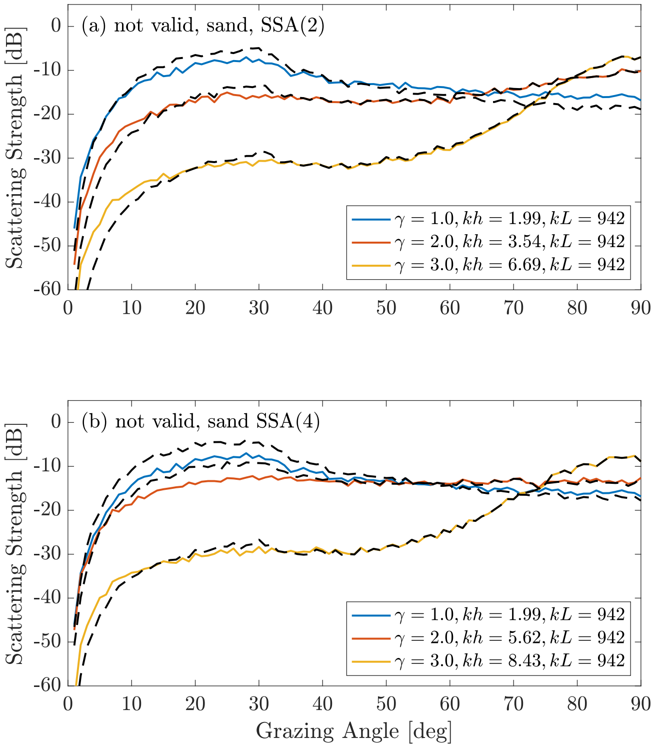

FIG. 3. Comparison between integral equation and small slope approximation (SSA(2) in (a) and SSA(4) in (b)) using the sand fluid-fluid boundary conditions for parameter combinations that are beyond the 1 dB validity criterion. Solid lines show the integral equation result, and dashed lines represent model results.

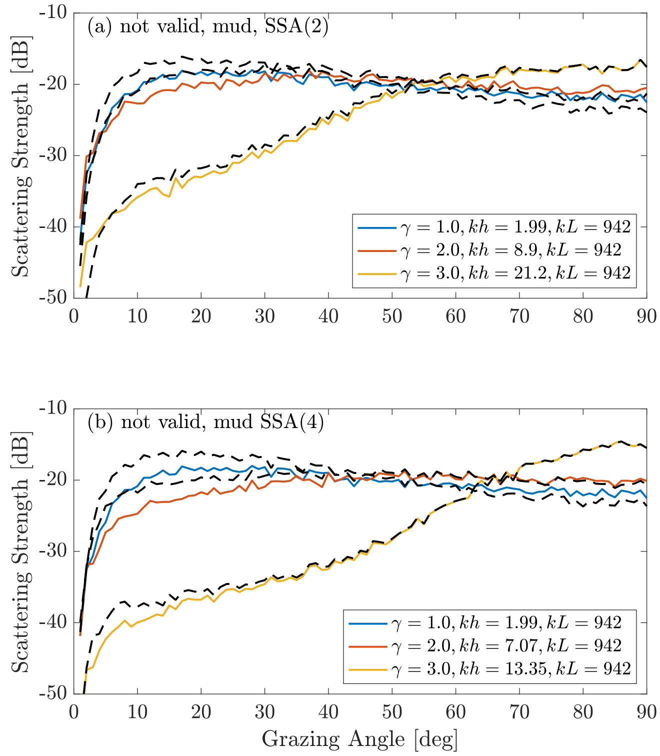

FIG. 4. Comparison between integral equation and small slope approximation SSA(2) in (a) and SSA(4) in (b) using the mud fluid-fluid boundary conditions for parameter combinations that are beyond the 1 dB validity criterion. Solid lines show the integral equation result, and dashed lines represent model results.

Fluid-fluid boundary conditions are presented next. In Fig. 3, comparisons between SSA(2) and IE results are shown in part (a) and the SSA(4) in part (b) for sand boundary conditions. As before, kh is about 2.5 times $kh_{\max}$ in each case. All of the model curves for SSA(2) and SSA(4) exhibit a local maximum near 31° grazing due to the critical angle. In the IE curves, the critical angle peak exists, but is a place where disagreement with the model is large. Disagreement between SSA(2) and field measurements has been seen recently by Hare et al.[33], where the measured scattering strength curve has shallower slope than the SSA(2) model (an effect also seen here). Similarly to the Dirichlet case, SSA(2) and SSA(4) disagree with the IE results at low angles for $\gamma = 3$, and at high grazing angles for $\gamma = 1$. Overall, the errors are not uniform in angle and the model tends to overestimate scattering strength near the critical angle, and underestimate scattering strength at high and very low grazing angles. Note that some cases here have a local minimum in scattering strength at the specular direction. This minimum is due to the Kirchhoff integral[67,68](related to the integral over x in Eq. 19), and can occur for very large spectral strength[41].

In Fig. 4, examples of IE, SSA(2) and SSA(4) are shown for the mud fluid-fluid boundary conditions for a value of kh that is 2.5 times that of the limit of validity (as before). The mud case does not have a critical angle in contrast to the previous example. Like the sand simulations, a local minimum in scattering strength near the specular direction is present for $\gamma < 3$. The kh values in Fig. 4 are far larger than either the sand or Dirichlet boundary conditions, because the corresponding $kh_{\max}$ values are larger. A major trend observed here is that the SSA(4) curves increase the error compared to SSA(2) for $\gamma > 1$ (since they have lower $kh_{\max}$). For $\gamma = 1$ both SSA(2) and SSA(4) give the same result.

B. Validity Bounds

The validity bounds, $kh_{\max}$ and $s_{\max}$ are examined in this section, and are shown as a function of the non-dimensionalized outer scale, kL, for different values of the spectral exponent, γ. The goal of this section is to observe trends in these two variables that can lead to an understanding of conditions under which the SSA(2) and SSA(4) are valid. Dirichlet boundary conditions are presented first, followed by fluid-fluid boundary conditions with sand and mud parameters.

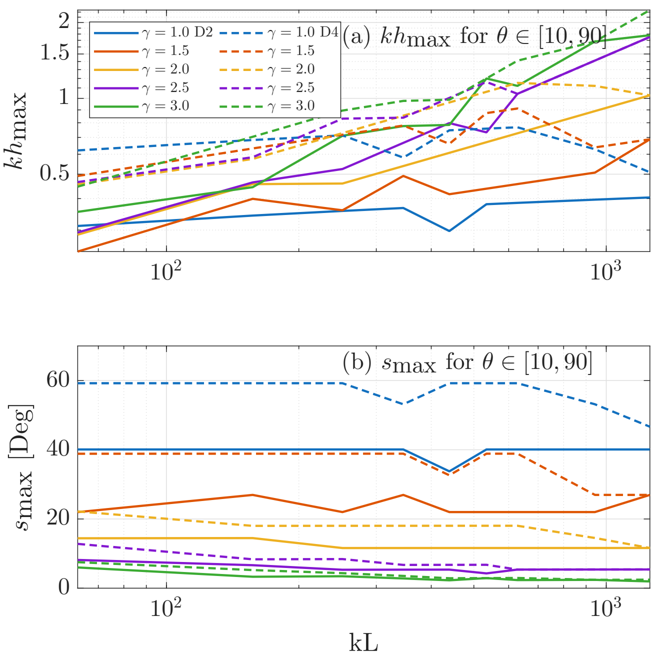

FIG. 5. Part (a) shows maximum valid rms height (non-dimensionalized by wave-number) for Dirichlet boundary conditions and backscattering angles between 10 and 90°. SSA(2) is shown in solid lines, and SSA(4) is shown in dashed lines. The color denotes different values of the spectral exponent, γ. Part (b) shows maximum valid rms slope for SSA(2) and SSA(4).

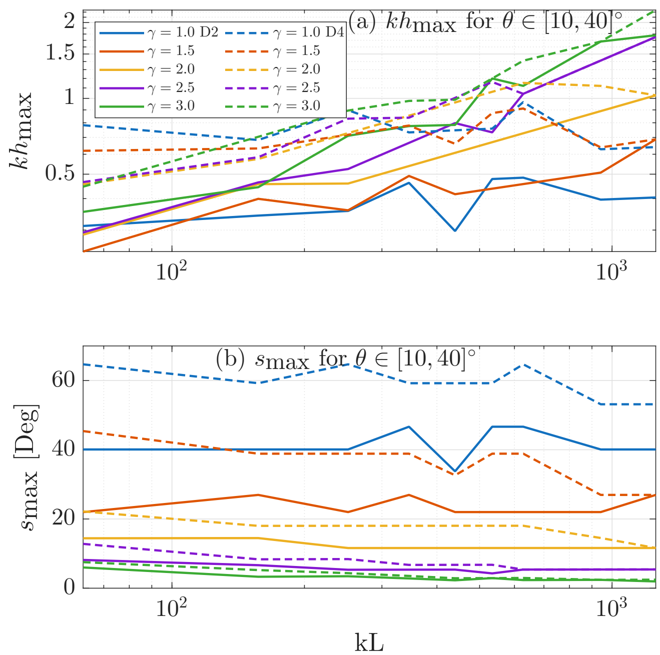

FIG. 6. Part (a) shows maximum valid rms height (non-dimensionalized by wave-number) for Dirichlet boundary conditions. These parameters are valid for low backscattering angles (between 10 and 40°). SSA(2) is shown in solid lines, and SSA(4) is shown in dashed lines. The color denotes different values of the spectral exponent, γ. Part (b) shows maximum valid rms slope.

1. Dirichlet Boundary Conditions

In Fig. 5, the validity criteria for all valid angles (between 10° and 90° grazing angle) are plotted for Dirichlet boundary conditions. Part (a) shows $kh_{\max}$, part (b) shows $s_{\max}$. The solid lines show the validity limits for each value of γ as a different color for SSA(2). Equivalent quantities for SSA(4) are shown in dashed lines. Note that $kh_{\max}$ versus kL is plotted on a log-log scale, and $s_{\max}$ versus kL is shown on a log scale for the horizontal axis, and in degrees rms slope on the vertical axis. The degree version of slope is $s_{\mathrm{Deg}} = 180/\pi \times \tan^{-1}(s)$. This transformation compresses the larger range of rms slopes. For example, rms slopes of 0.5, 1 and 2 are 25°, 45°, and 63° respectively. This compression is useful for graphical analysis, and has been used extensively in the literature on scattering model validity[10,21,35].

Overall, the validity limit is larger as kL increases. The slope of this line is steeper for large γ than it is for small γ. The validity limit for SSA(4) is larger than for SSA(2), although in a few isolated points they are equal (such as $\gamma = 2$ for the largest value of kL). It is possible that a statistical error due to finite ensemble size is responsible for these cases. Most of the $kh_{\max}$ values are on the order of 1, with smaller γ and smaller kL being slightly less than 1, and $\gamma \geq 2.5$ and $kL > 700$ being slightly greater than one. $kh_{\max}$ is never greater than 2 for the cases examined in this work, and the smallest value is about 0.1. Extrapolating to larger and smaller values of kL suggests that these are not absolute limits. It is remarkable that the values of $kh_{\max}$ are so close to each other for a diverse set of power law parameters. In contrast, the corresponding values of $s_{\max}$ in part (b) are widely different in magnitude as γ varies, but approximately constant as a function of kL. Large values of γ have $s_{\max}$ on the order of a few degrees, whereas for $\gamma = 1$, $s_{\max}$ is around 40° for SSA(2) and 50-60° for SSA(4). On average, SSA(4) for Dirichlet surfaces has $kh_{\max}$ and $s_{\max}$ (units of slope) approximately 1.75 times that of SSA(2). The different behavior for $kh_{\max}$ and $s_{\max}$ is due to the dependence of h and s on kL, γ, and w.

Similar plots for $kh_{\max}$ and $s_{\max}$, but only for low backscattering angles between 10 and 40 degrees grazing are shown in Fig. 6. Overall, the bounds are very similar to the previous figure that used all valid angles. One notable difference occurs for $\gamma = 1$, where the small kL region has a higher $kh_{\max}$ at low angles than for all angles. Examination of the model-IE comparison in Fig. 2 for $\gamma = 1$ shows that the error is much larger at normal incidence than at grazing. Therefore, if the near specular region is ignored (as it is for small grazing angles in Fig. 6), then $kh_{\max}$ will be slightly larger.

A version of the validity plots for high backscattering grazing angles between 70 and 90 degrees is shown in Fig. 7. In this case the $\gamma = 1$ curve is almost the

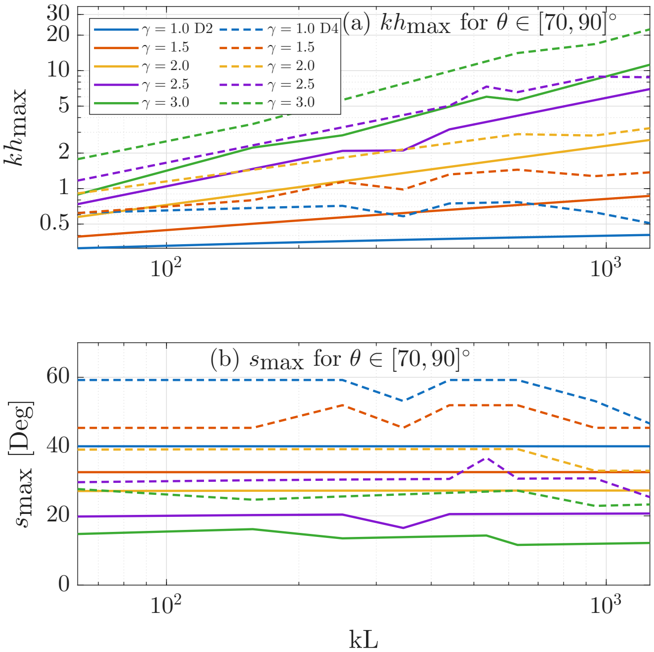

FIG. 7. Part (a) shows maximum valid rms height (non-dimensionalized by wave-number) for Dirichlet boundary conditions. These parameters are valid for high backscattering angles (between 70 and 90°). SSA(2) is shown in solid lines, and SSA(4) is shown in dashed lines. The color denotes different values of the spectral exponent, γ. Part (b) shows maximum valid rms slope.

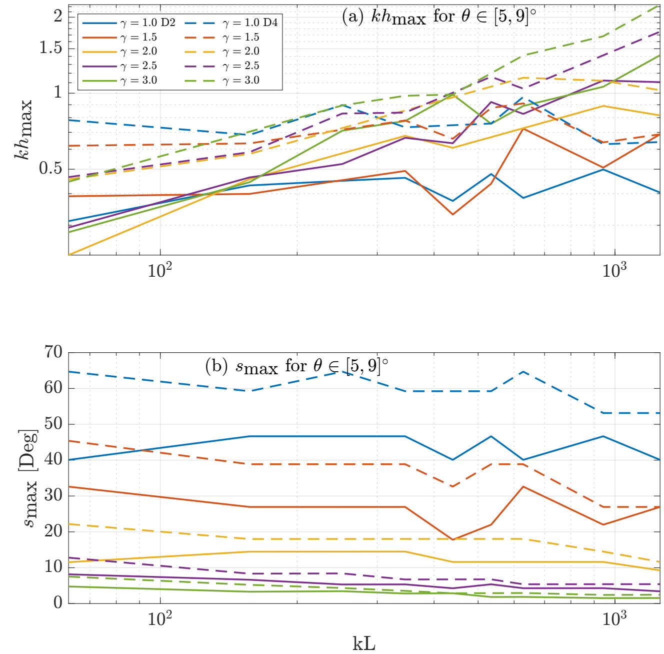

FIG. 8. Part (a) shows maximum valid rms height (non-dimensionalized by wave-number) for Dirichlet boundary conditions. These parameters are for very low backscattering angles (between 5 and 9°). SSA(2) is shown in solid lines, and SSA(4) is shown in dashed lines. The color denotes different values of the spectral exponent, γ. Part (b) shows maximum valid rms slope.

same as for all angles in Fig. 5, since the error mostly concentrated near the specular direction for this spectral exponent. The larger values of γ are much different. In these cases, the kh_{max} and s_{max} are much larger for steep angles than they are for shallow angles. In other words, the small slope approximation can tolerate much higher rms height and spectral strength near the specular direction when γ is large. Broschat and Thorsos[35] and Wang and Broschat[36] also found that the small slope approximation was more accurate (had a higher maximum kh and s) near the specular direction for bistatic scattering, using Gaussian and Pierson-Moskowitz roughness spectra respectively.

For steep angles and SSA(2), s_{max} is more or less constant with kL, although the SSA(4) appears to have a slightly smaller s_{max} for the larger values of kL. Neither kh_{max} nor s_{max} are clustered around a single order of magnitude when considering variations in both kL and γ, although s_{max} is largely insensitive to kL. We observe kh_{max} values up to about 20, and as low as 0.2. The RMS slope limitations were as high as 60 ° for SSA(4) and 40° for SSA(2), and as low as about 10° for SSA(4) and 30° for SSA(2).

Very low grazing angle backscattering situations are of consequence for long-range reverberation scenarios. In these numerical simulations, the incident field has a finite angular width due to the taper, and this width becomes as large as 50% of the grazing angle when $\theta = 5°$. A conservative bound on the lower limit of the grazing angles accessible by this study is therefore 5°. The validity region for very low grazing angles is shown for kh and s in Fig. 8. This plot is similar to Fig. 6 for angles between 10° and 40°, except that on average kh_{max} for $\gamma = 1$ is 1.1 times larger for very low angles, and for $\gamma = 3$ is 0.87 times as large. Smaller grazing angles require much longer surface lengths. To deal with these large simulations, approximate methods such as the fast multipole algorithm would be needed[45].

2. Fluid-fluid boundary conditions

Next, fluid-fluid boundary conditions are examined in Fig. 9. The parameters kh_{max} and s_{max} are shown in the same format as previously. Overall for SSA(2), the validity region is slightly larger (about 1.9 times for kh_{max}) for sand than for Dirichlet boundary conditions. The largest value of kh_{max} is approximately 3, and the smallest is approximately 0.6. Similar trends are observed for the kL dependence as for the Dirichlet case. The slope of the sand kh_{max} versus kL is about the same for $\gamma = 1$ as it is for the Dirichlet case, but is less steep than the $\gamma = 3$ Dirichlet case.

In contrast to the Dirichlet examples, SSA(4) for sand has higher kh_{max} and s_{max} only for large values of γ. When $\gamma \leq 1.5$ it either has the same maximum parameter as SSA(2), or is slightly lower. For $\gamma > 1.5$, the SSA(4) $kh_{\max}$ is only slightly larger than SSA(2) on average. This effect may be due to not all terms up to fourth order in slope being included in the SSA(4) form used here (see Sec. VI C for a discussion of this). It is interesting to note that for $\gamma = 1$, $s_{\max}$ for SSA(2) is about 60 degrees, which is the value for SSA(4) for Dirichlet boundary conditions.

The validity limits for low angles only are not shown here because they are exactly the same as the results already shown for all angles in Fig. 9. For high grazing angles, the trends are similar to the Dirichlet case and are not shown for brevity. At high angles, $kh_{\max}$ and $s_{\max}$ are larger by a factor of 2.4 on average for SSA(2) compared to Dirichlet boundary conditions and larger by a factor of 1.6 for SSA(4).

The parameters $kh_{\max}$ and $s_{\max}$ are shown for mud in Fig. 10, with the same presentation format as before. The overall trends with γ and kL are similar to the previous figures, although the precise values are higher than either the sand or Dirichlet cases. The maximum valid kh for SSA(2) in these simulations was approximately 11. The largest valid s was approximately 60 degrees (for both SSA(2) and SSA(4)), and occurred for $\gamma = 1$. This was the same value found for sand for SSA(2), and Dirichlet for SSA(4). For $\gamma = 1$, the extra term makes no difference to $kh_{\max}$ compared to SSA(2). At all other values of γ, $kh_{\max}$ is smaller for SSA(4) than it is for SSA(2), meaning that the extra term introduces error (see Section VI C). The maximum $kh_{\max}$ in these simulations was 7 for SSA(4), and is on average 0.80 times that of SSA(2) for mud.

At low backscattering grazing angles, SSA(2) for mud has the same $kh_{\max}$ as for all angles. For high angles, $kh_{\max}$ for SSA(2) is again larger, this time a factor of 3.4 times larger than Dirichlet SSA(2) high angles, and 1.5 times larger compared to sand SSA(2) at high angles. The maximum $kh_{\max}$ at high angles in the cases examined is 56 for $\gamma = 3$, and the smallest is 1 for $\gamma = 1$. In this angular range, $s_{\max}$ is between 46 and 69 degrees depending on the value of γ. For SSA(4), $kh_{\max}$ is larger at steep angles than it is for SSA(2), by a factor of 3.3. At low angles SSA(4) has the same validity limits as SSA(4) at all angles, since most of the error is at small grazing angles.

VI. DISCUSSION

In this section, the trends seen for $kh_{\max}$ and $s_{\max}$ as a function of kL, θ, γ, and boundary condition are discussed. Comparisons are made to other studies of the SSA for Dirichlet boundary conditions. The potential reasons as to why SSA(4) does not always provide an improvement over SSA(2) are discussed. Comparisons to other scattering models (specifically PT and the KA) are made, underscoring the attractiveness of the SSA. Large roughness effects such as backscatter enhancement and the applicability of Lambert's law are discussed. Since $kh_{\max}$ and $s_{\max}$ are related through the power law parameters, $kh_{\max}$ is used to stand in for both in this section, unless $s_{\max}$ is explicitly stated.

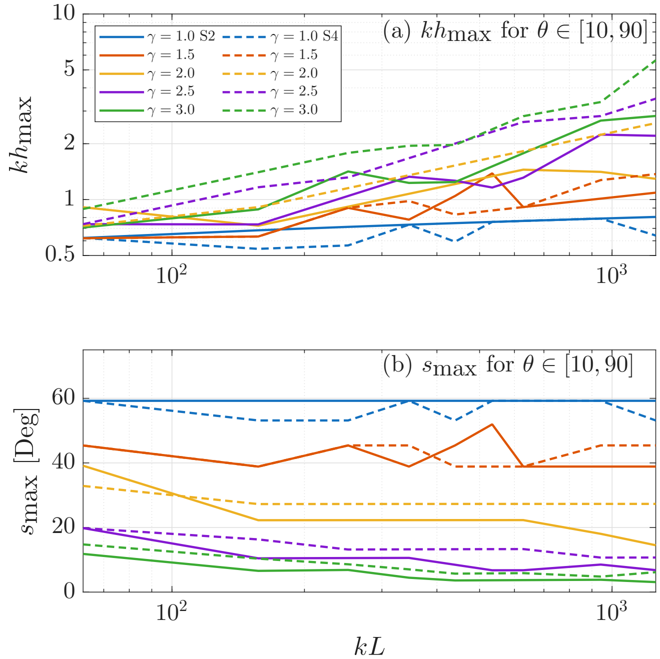

FIG. 9. Part (a) shows maximum valid rms height (nondimensionalized by wave-number) for fluid-fluid sand boundary conditions and both SSA2 (solid) and SSA(4) (dashed). These parameters are valid for all valid backscattering angles (between 10 and 90°). The color denotes different values of the spectral exponent, γ. Part (b) shows maximum valid rms slope for the same models and boundary conditions.

A. Angular and kL dependence of $kh_{\max}$

It is first noted that for SSA(2), $kh_{\max}$ increases with kL, and near-specular backscattering angles have a higher $kh_{\max}$ than medium or near-grazing angles (for $\gamma > 1$). It is assumed here that SSA(2) is accurate when the extra contribution to SSA(4) is small relative to SSA(2). Furthermore, if the extra contribution to SSA(4) grows with kL more slowly than relative to the dependence of SSA(2) on kL, then it is possible to explain the dependence of $kh_{\max}$ on kL for SSA(2).

This relationship can be explained by examining the relative contribution to the T_1 term in the SSA series in comparison with T_0. Recall that expressions for T_0 and T_1 is given in Eqs. (19) and (20). Let

$$u = \frac{\Phi_1}{k\Phi_0} = \frac{\tilde{A}_2 + i\nu_z A_1}{2kA_1} \tag{34}$$

be a nondimensional version of the wavenumber integrand multiplying F and the exponential in the expression for T_1. This quantity is normalized by Φ_0, so it expresses the contribution to the second term in the SSA series relative to the first, without taking into account the roughness spectrum.

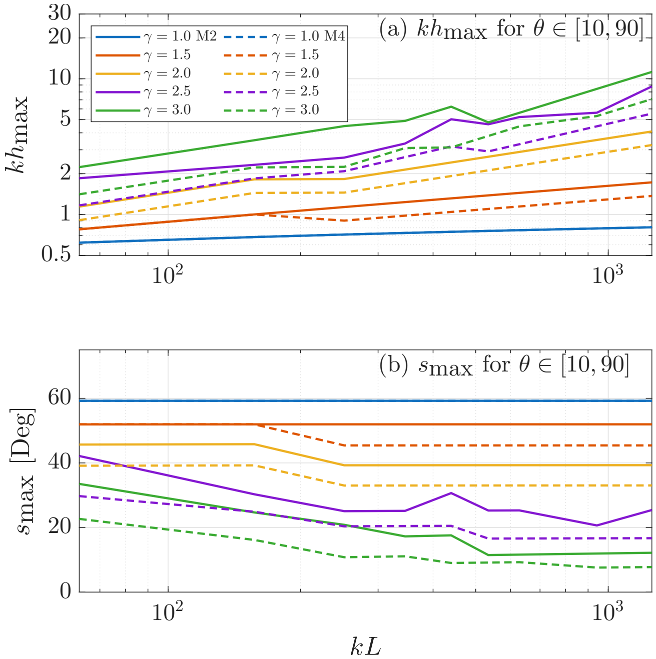

FIG. 10. Part (a) shows maximum valid rms height (non-dimensionalized by wave-number) for fluid-fluid mud boundary conditions and both SSA2 (solid) and SSA(4) (dashed). These parameters are valid for all valid backscattering angles (between 10 and 90°). The color denotes different values of the spectral exponent, γ. Part (b) shows maximum valid rms slope for the same models and boundary conditions.

The integral over k_{1x} in the expression for T_1 is proportional to the inverse Fourier transform of F weighted by this function u. Most of the contribution to the mean square height comes from the low wave-number components near k_L. The function u as a weighting function controls which portions of the roughness spectrum contribute most to T_1. The non-dimensional quantity u is plotted as a function of nondimensional k_{1x} in Fig. 11 for three backscattering situations, $\theta = 20°$, $60°$ and $90°$ in each subfigure, and the three boundary conditions as different line styles. When $|k_{1x}|$ is sufficiently large, $|u|$ behaves like a linear function. The weighting function u therefore emphasizes high wave-number components, and for asymptotically high frequencies, behaves like a derivative filter, as discussed by Broschat and Thorsos[35]. This is one of the reasons that the small slope T-matrix series is in powers of generalized slope[14,57].

Due to this filter, low wave-number parts of the power spectrum have a small weight in the Fourier integral compared with large wave-numbers. Therefore, as kL increases, the main portion of the rms height is due to low wave-number components of the roughness power spectrum, but they have progressively smaller weights as $1/L$ tends to zero. Therefore, the weighting function should result in larger $kh_{\max}$ as kL becomes larger, which was observed for all boundary conditions. The value of γ has a significant effect here. For $\gamma = 3$, a large fraction of the contribution to h occurs for small wave-numbers, and it should have the largest $kh_{\max}$ for the simulations examined here (seen in Figs. 5-10). Empirically, it is found that when kL is greater than a certain value, w_{max} is approximately constant as a function of kL, which shows the effect of the filter u. For $\gamma = 1$, the dependence of kh on kL is logarithmic, and should therefore have the smallest $kh_{\max}$, which was observed empirically in this work.

Next, we turn to the result that $kh_{\max}$ is often larger for near-specular backscattering angles than for near grazing angles. The function u is zero when $k_{1x} = 0$, as demanded by the SSA[14,57]. For small $|k_{1x}|$, its behavior depends on the backscattering angle. Fig. 12 plots u for three different angles on a log-log scale, as a function of k_{1x}/k. Notably, the 90° backscattering curve is smaller than the others, and has the steepest slope of 2 (or k_{1x}^2) near the origin, and the curves for the two non-specular grazing angles have a slope of 1 (k_{1x}^1) near the origin. All curves converge to approximately the same power law behavior of k_{1x}^1 at very high wave-numbers, and have almost the same magnitude. Note that not all of the curves in Fig. 12 show a slope of 1 at high wavenumbers, but it is acheived when k_{1x}/k is examined for values higher than the figure's upper limit of 4. Due to the small magnitude of u, and larger power-law exponent near the origin, u for near-specular angles has a very small weight applied to the low wave-number portion of the power spectrum compared to moderate or near-grazing angles. Therefore, near specular, SSA(2) should have a larger $kh_{\max}$ compared to other angles. Again, this effect is dependent on γ, with much higher $kh_{\max}$ near the specular direction observed for large spectral exponent, and almost the same $kh_{\max}$ observed for small exponent, when compared with lower angles.

B. Boundary conditions

The effect of boundary conditions on $kh_{\max}$ is significant. We found that for SSA(2), the Dirichlet boundary condition had the smallest $kh_{\max}$, followed by sand, followed by mud (holding all other parameters constant). The mud boundary condition had the smallest contrast between the two media (the sound speed ratio was nearly one, and the density ratio was the closest to one). Of the two types of boundary conditions examined here, only the Dirichlet is impenetrable, meaning that sound is scattered entirely back into the acoustic medium. It is generally understood that the stronger the contrast of a fluid interface, the less penetrable the interface is to sound. This leads to the hypothesis that weaker contrasting interfaces will have higher $kh_{\max}$ for SSA(2) than strongly contrasting ones. This hypothesis can be put on more solid footing by examining Fig. 11. In each subfigure, u is plotted for different boundary conditions. The lowest curve is mud, followed by sand, followed by Dirichlet. This ordering is the same as $kh_{\max}$ from the integral equation results, and therefore we can tentatively provide some evidence to support this hypothesis. The precise

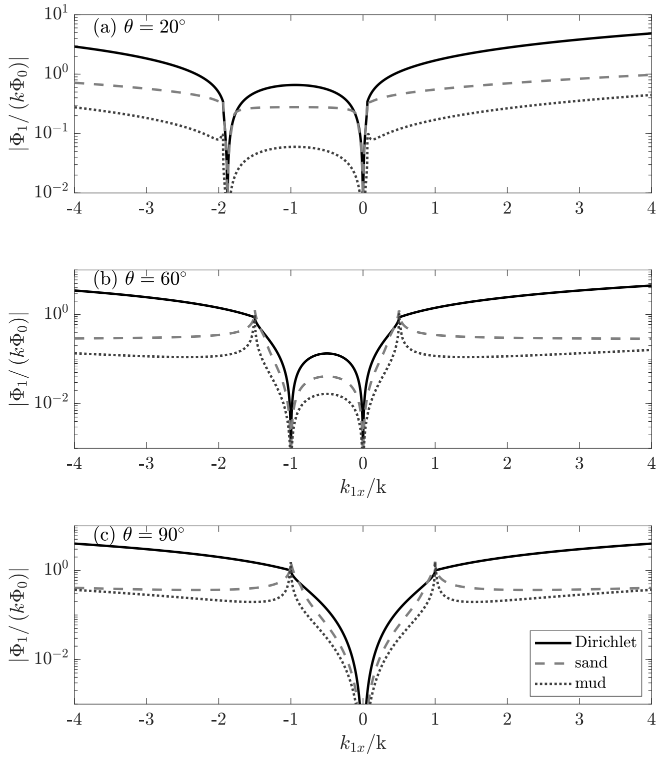

FIG. 11. The magnitude of k_{1x} integrand function Φ_1 for T_1^{SSA} divided by the coefficient for T_0^{SSA}. This quantity is plotted for three different boundary conditions, Dirichlet, sand, and mud (noted in the legend). Part (a) shows this function for low backscattering grazing angle, 20°, part (b) shows 60°, and part (c) shows 90°.

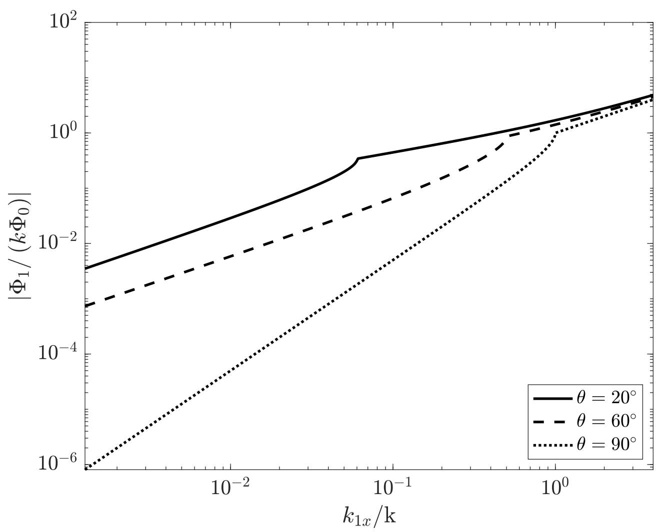

FIG. 12. A plot of the magnitude ratio of Φ_1/Φ_0 for Dirichlet boundary conditions using log-log axes. The plots show three angles (noted in the legend), with the curve for 90° grazing having a slope of 2 near the origin. The rest have a slope of 1.

role of a_c, a_ρ, and the attenuation parameter δ has not been identified, but the information is contained in the formulae for $\tilde{A}_2$ and A_1.

C. SSA(4) is not always a better approximation

In the Dirichlet boundary condition, SSA(4) almost always resulted in higher $kh_{\max}$ than SSA(2). The same was not true for the fluid-fluid boundary conditions. The most obvious reason this might be the case is that the form of SSA(4) used in this work is not the full scattering cross-section to fourth order in generalized slope. It is missing the cross term $T_0T_2^* + T_2T_0^*$, which was neglected due to its computational complexity, and because Broschat and Thorsos[35] give an argument that the sum $T_0 + T_1$ reduces to the Kirchhoff approximation for asymptotically large k, which is an attractive property. Further investigation of the full fourth order SSA for power-law surfaces may yield an improvement in fluid-fluid cases.

If the form of SSA(4) is an accurate expression to fourth-order in rms slope, then another explanation is needed. It is first noted that $kh_{\max}$ for SSA(2) is larger for the fluid-fluid boundary conditions than Dirichlet. Given that the validity limits for SSA(2) are already high (for some fluid-fluid cases), we speculate that the small slope series may require higher order terms in generalized slope (e.g. to fifth or higher order). In the case of mud and SSA(2), $s_{\max}$ is already greater than unity (in units of slope) for smaller values of γ, and $kh_{\max}$ is larger than unity for larger values of γ. These large parameters may prevent either the small slope or perturbation series from being accurate at fourth order. Although the small slope approximation is formulated independently of kh, a finite number of terms are used in the perturbation series to determine the coefficients Φ_n. For example, T_0 uses the first two terms in the perturbation series, and T_1 uses the first three. All the SSA(2) mud cases for which either $kh_{\max} > 1$ or $s_{\max} > 45°$ have a poorly (or neutrally) performing SSA(4). It may be the case that if the SSA series were calculated to higher orders (including T_2, T_3 etc.), some improvement may be possible for the mud boundary condition, and for the case of $\gamma = 1$ for sand.

It may also be that the small slope series itself diverges for these large values of $s_{\max}$ and $kh_{\max}$, and the only usable term is the lowest order. It is also interesting to note that the largest rms slope tolerated by SSA(4) for Dirichlet boundary conditions, SSA(2) for sand, and SSA(2) for mud is approximately 1.73 (60°). This similarity between s_{max} in these cases may suggest an upper bound to the slope tolerated by the small slope series as a whole, although future work is needed to confirm or refute this speculation. Divergence of a series has been observed in other scattering models, and is a motivation for our hypothesis. Previous numerical work has shown that the perturbation series has a maximum slope beyond which the series diverges for sinusoidal roughness[69]. Note that the slope limitation in perturbation theory is not related to the Rayleigh hypothesis, but an implicit series in slope due to the Taylor expansion of the Green's functions (See Voronovich[56] pages 81-83). The small slope approximation is also a local approximation, because it does not explicitly contain multiple scattering[70]. Multiple scattering may be a reason that the SSA series does not converge. The non-local SSA may be able to model very large roughness cases studied here[71]

D. Comparison to other studies of the SSA

It is interesting to compare these results to the findings of Broschat and Thorsos[35]. In that work, a Gaussian roughness spectrum model was used, with length scale L_G. The Gaussian spectrum is highly concentrated at zero wave-number and had very little energy for wave-numbers greater than about $2\pi/L_G$. They found that as kL_G was increased, the error compared with the IE result for SSA(2) and SSA(4) increased, especially for the backscattering direction. This result is the opposite of the findings of this work, where increasing kL with a fixed kh leads to a smaller error, noting of course that L is not the same as L_G.

This discrepancy can be explained by the fact that the Gaussian rough surface is a single-scale surface, whereas the power law model is multiscale and the roughness power is more evenly distributed over the domain of support. Consider the case of large kL_G and large kL, and small θ so that the incident and scattered wavenumbers have magnitudes close to k, and the Bragg wavenumber, $k_b = 2k\cos\theta$ is approximately $2k$. For very small grazing angles in the backscattering direction, perturbation theory is accurate whenever SSA(2) is accurate (see Figs. 13 and 14 below). Perturbation theory predicts that the scattered intensity is proportional to $W(k_b)$. The next term in the SSA series uses an integral of the roughness spectrum weighted by u and the exponential term.

A Gaussian roughness model is sharply peaked around the origin for large kL_G, and the spectral levels are small at the Bragg wavenumber compared to the peak. Therefore, for large kL_G (and therefore large k_bL_G), the integral over k_{1x} will have significant contributions in T_1 compared to T_0. In contrast, the power-law model is not as sharply peaked as the Gaussian model. If we set $kL = kL_G = 10$, then the ratio of peak spectral density to the value of the Bragg wave number is approximately 10^{43} for the Gaussian surface and between 3 and 32 for the power law model γ with 1 and 3 respectively. As noted earlier, the function u gives a low weight to small wavenumber components, but it is not a small enough weight to compensate for 43 orders of magnitude of difference in the Gaussian model. Therefore, large values of kL_G produce much different behavior for the validity of the SSA for Gaussian surfaces than for the power-law model for similar L and L_G. These different ratios are a consequence of the single-scale nature of the Gaussian roughness model, and the multiscale, broadband nature of the power law model.

It is also instructive to compare to a study of SSA validity for the Pierson-Moskowitz roughness spectrum by Wang and Broschat[36]. This spectrum has a power law form with an exponent of 3 at high wave-numbers, and has a lower-frequency cutoff, K_p. Both h and K_p are controlled by the wind speed[34], U, with $h \propto U^2$ and $K_p \propto U^{-2}$. This model is similar to the $\gamma = 3$ case of the power-law model, but without the independent control of spectral strength and low wave-number cutoff. Wang and Broschat[36] have broadly similar conclusions as this work. For incident angles near the specular direction, SSA(2) can tolerate rather large kh, and maximum valid kh decreases for small grazing angles. Extremely large values of $kh \approx 134$ were found to be accurately modeled by SSA(2) for the Pierson-Moskowitz near the specular direction, which is much higher than the values observed in this work. These precise values should be used with caution, as the sampled surfaces in Ref. 36 are not long enough (especially in their electromagnetic simulations) to adequately capture the low wave-number peak K_p that drives much of the rms roughness, and are therefore overestimates of h.

E. Comparison to other approximations

The lowest order SSA has been described as being accurate over a larger angular domain than either PT or the KA[6]. The numerical simulations in this work can be used to support this claim. The T-matrix for PT can be derived from the SSA T-matrix (Eq. 19) by performing a Taylor expansion of the $\exp(-i\nu_z f(x))$ term resulting in $1 - i\nu_z f(x)$. The KA formula for T_0 for one dimensional roughness is[6,21]

$$T_0^{KA} = \frac{V_{ww}(\theta_{is})}{k}\left(k_{ix}\frac{\Delta k_x}{\Delta k_z} + k_{iz}\right)\int dx e^{i\nu_x x - i\nu_z f(x)}\,, \tag{35}$$

where $V_{ww}(\theta_{is})$ is the flat-interface reflection coefficient evaluated at the angle[6]

$$\theta_{is} = \sin^{-1}\left(\sqrt{\Delta k_z^2 + \Delta k_x^2}/2k\right).$$

A comparison between SSA(2), PT, and KA for sand boundary conditions is shown in Fig. 13. In each case, parameters that just satisfy validity for SSA(2) are shown, and different values of the spectral exponent are shown in each sub-figure. Part (a) shows $\gamma = 1$. While SSA(2) is accurate over all angles, PT overestimates the cross-section for angles above about 60° grazing angle, and KA underestimates the scattering cross-section for angles less than 70° grazing angle, and overestimates for very low grazing angles. In part (b) the spectral exponent is increased to 2. Here, the KA still underestimates the scattering cross-section for angles less than 70° grazing angle, but PT diverges from the IE result only for angles greater than 80° where it overestimates the scattering cross-section. As the spectral exponent increases to 3 in part (c), the KA is still accurate for grazing angles greater than 70°, but PT underestimates the scattering cross-section above 80° grazing angle, and overestimates for angles very close to specular. The PT scattering strength is extremely small exactly at the specular direction because there is negligible power spectral density at zero wavenumber (i.e. the Bragg wavenumber for the specular direction) for the truncated power law model. For all of the PT results here, most of the error is near the specular direction, and the converse is true for KA. These conclusions agree with speculative statements in the literature about these models (see Ch 13 of Jackson and Richardson[6], especially Fig. 13.2).

A reliable lower limit for the validity of the KA for backscattering appears to be 70°. This limit holds for all angles of w (up to the limit of KA as a whole) and for both sand and mud boundary conditions. Increasing or decreasing spectral strength does not appreciably expand or shrink the angular region for which the KA is accurate, although the KA has the same upper limit of w as does the SSA(2) near the specular direction. Although PT is generally accurate for small to moderate grazing angles, there are isolated angles where the error jumps above 1 dB at small and moderate angles. This phenomenon is because higher order terms in the series for $\exp(-i\nu_z f(x))$ may provide small corrections at small and moderate grazing angles that improve the model-data comparison. These terms are included in SSA(2), but not PT.

A graphical depiction of the validity regions for these models are given in Fig. 14. The spectral exponent is held constant at 2, and $kL = 400\pi$. Each sub-figure shows whether a particular angle and spectral strength combination is valid (gray), overestimated by the model (white), or underestimated by the model (black). The latter two cases are different ways for the model to be invalid, and also use the 1 dB criterion. Spectral strength is plotted as the decibel version of w non-dimensionalized by $k^{3-\gamma}$. Part (a) shows SSA(2) as a reference. The domain of validity of PT in part (b) is a subset of SSA(2). Errors close to the specular direction, and isolated errors at small and moderate grazing angles can be seen. Part (c) shows the Kirchhoff approximation, and its validity region in this parameter space is approximately rectangular. The limit of 70° is remarkably constant as a function of spectral strength. Small deviations from this shape are seen for other values of γ, but are not plotted here for brevity.

The shape of the valdity region for SSA(2) is rather complicated compared to that of the KA. Near the specular direction, it has the same behavior as the KA. However, away from the specular direction at large values of w it has a region where it overestimates the scattering strength. This region is near the critical angle. Similar behavior can be seen in Fig. 3 where there is a small angular region where SSA(2) over estimates near the critical angle, and underestimates near the specular direction. At very low grazing angles both PT and SSA(2) underestimate the scattering cross section.

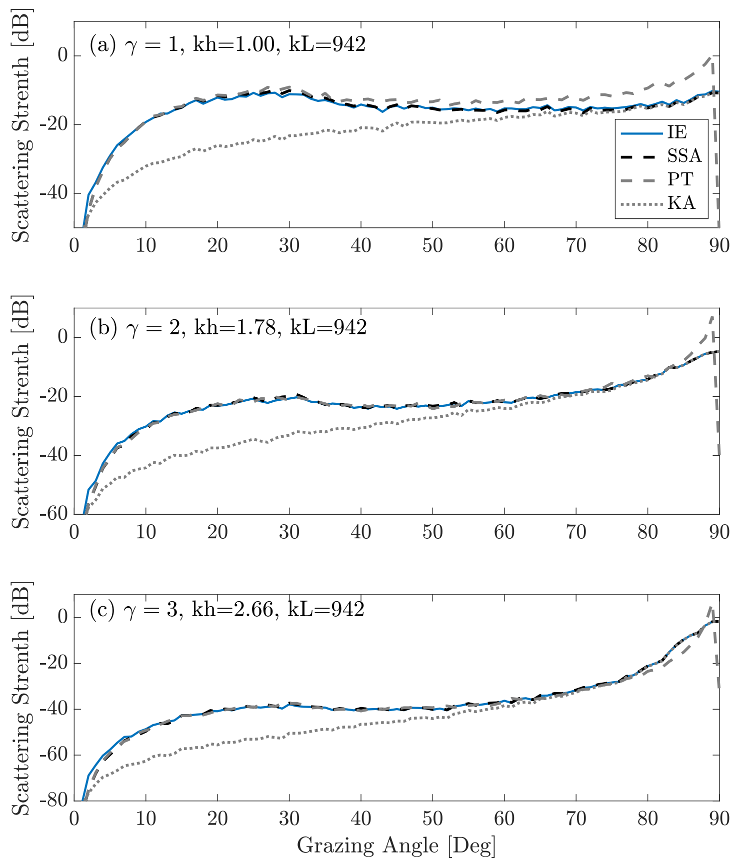

FIG. 13. A comparison of scattering strength calcuated between several methods, the integral equation result, SSA(2), KA and PT. Each subfigure shows a different value of γ.

F. Backscatter enhancement

In some previous numerical studies of scattering from very rough surfaces with a Gaussian roughness spectrum, a peak in the backscattering direction was found in the bistatic scattering cross section[72,73]. This peak has been termed backscattering enhancement, and is due to multiple scattering[70], which is an iterative extension of the tangent plane approximation. Since the backscattering direction contains double-scattering paths that are reciprocal and thus coherent, enhanced scattering in the backscattering direction is possible. Since the small-slope approximation is a local scattering approximation (i.e. it ignores multiple scattering)[74], it is natural to examine the bistatic field to determine whether backscatter enhancement exists, which would indicate the presence of significant multiple scattering. As stated earlier, multiple scattering may be potential cause for failure of the small slope series to converge.

Several examples of the bistatic scattering cross-section for the largest spectral strengths used in numerical simulations are presented for the Dirichlet boundary condition in Fig. 15. The upper row of this figure shows the bistatic scattering cross section for a spectral exponent of two, an rms slope of 69°, and $kh = 9$. Increasing

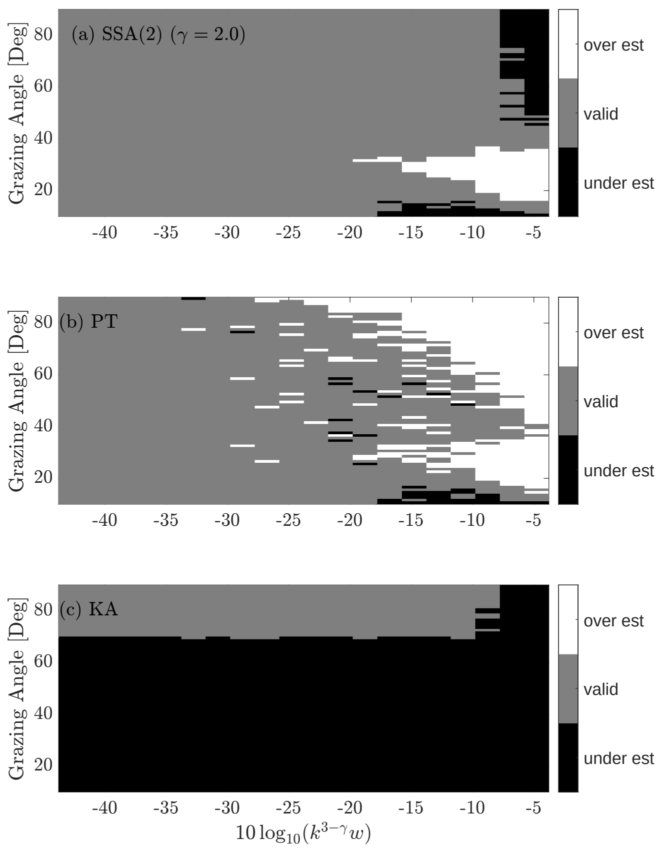

FIG. 14. Model validity is presented as a function of spectral strength and grazing angle for the three different approximations. The roughness parameters were $\gamma = 2$, $L/\lambda = 200$, and geoacoustic properties for sand were used. The spectral strength shown as the decibel version of the nondimensional quantity $k^{3-\gamma}w$.

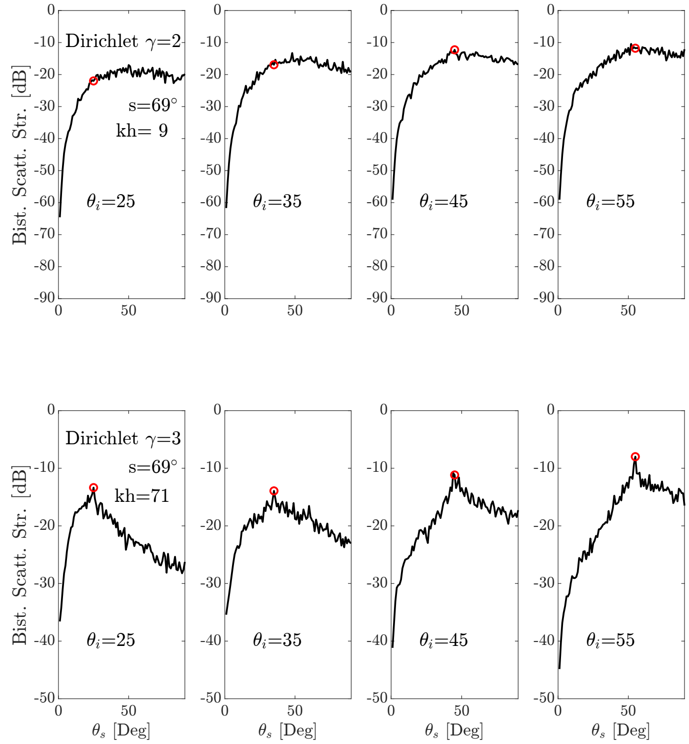

FIG. 15. The bistatic scattering cross-section for the Dirichlet boundary conditions with various incident grazing angles is shown for two different roughness properties. The top row shows cases with a spectral exponent of two, and the bottom row has an spectral exponent of three. Different values of the incident grazing angle are shown in each row. The backscattering direction is denoted by the red circle. Narrow peaks in the bottom row indicate backscatter enhancement.

values of the incident grazing angle are used for each column. The scattered grazing angle is indicated on the horizontal axis. A red circle indicates the backscattering direction. No obvious peaks in the numerical experiment are present. The lower row shows the bistatic scattering strength for a spectral exponent of three, the same value of rms slope, but now $kh = 71$. In the lower row, a narrow peak is observed near the backscattering direction. For the smallest incident grazing angle (25°), both a narrow peak and a broad peak are visible near the backscattering direction. The broad peak is likely not due to backscattering enhancement, and may be related to the specular minimum predicted by the Kirchhoff integral[67].

Backscattering enhancement, and therefore multiple scattering is present for power-law roughness with large root mean roughness and large root mean square slope. The rms slope needed to observe backscattering enhancement is larger in this work than for Gaussian roughness. It is hypothesized that these differences in kh and s are due to the broadband nature of power law roughness, and that the presence of significant rms roughness at scales near the wavelength can disrupt the mechanism responsible for backscatter enhancement. It seems necessary that both large s compared to the incident grazing angle, and large kh are present. The presence of multiple scattering in these simulations may indicate a possible reason that SSA(2)[14] fails for large roughness. Future efforts to model scattering from power-law rough surfaces may need to take multiple scattering into account, e.g. using the non-local small slope approximation[71].

G. Applicability of Lambert's law

Lambert's law was originally developed to model the angular dependence of light scattering from the surface of the Moon[75 76]. It has commonly been used to model scattering from very rough surfaces at small to moderate grazing angles[44,77,78]. The form for the monostatic Lambert model is $\sigma = \mu \sin^2\theta$, where μ is Lambert's parameter and is empirically determined. A generalization of Lambert's law, $\sigma = \mu_p \sin^p\theta$ was suggested by McKinney and Anderson[79], with p as a free parameter. Setting $p = 2$ corresponds to the Lambert model, $p = 1$ corresponds to the Lommel-Seeliger model (backscattering only)[80–82], and $p = 3.3$ was used in the empiri-

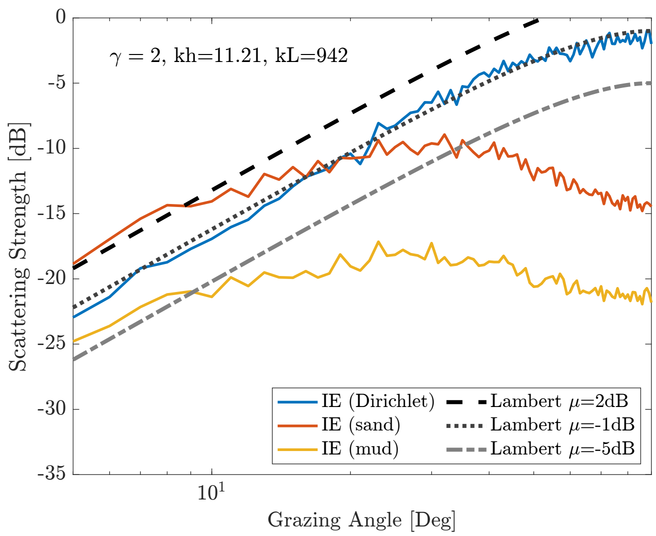

FIG. 16. Comparison of scattering strength for the Dirichlet, sand and mud boundary conditions for large kh and kL and $\gamma = 2$ to Lambert's law.

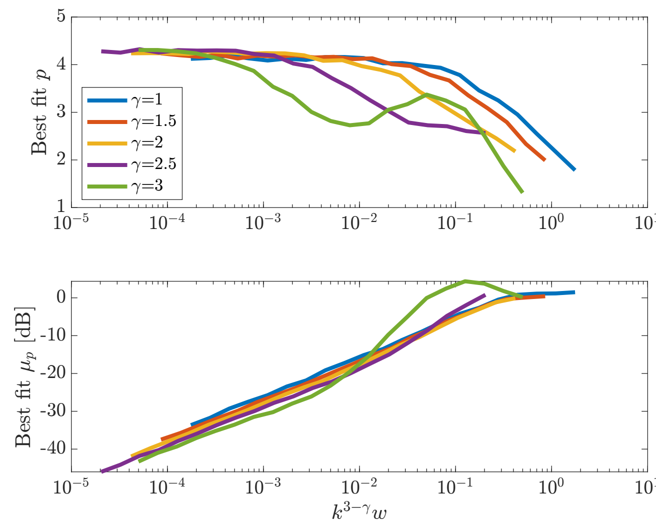

FIG. 17. Results of fitting the generalized Lambert model to Dirichlet integral equation simulations between 5 and 40 degrees grazing angle. Parameters are the exponent, p and the coefficient, μ_p with units of decibels. The horizontal axis is $wk^{3-\gamma}$.

cal Chapman-Harris model for scattering from the sea surface[83].

A comparison of the scattering strength for different boundary conditions to Lambert's law for very rough surface parameters and $\gamma = 2$ is given in Fig. 16. Overall, the Dirichlet results compare very well with Lambert's law for a wide variety of angles. The sand boundary conditions only compare favorable with Lambert's law for very small grazing angles, and the mud boundary condition has a shallower slope than Lambert's law at very small angles.

Note that the Lambert parameters in Fig. 16 and the largest generalized Lambert parameters in Fig. 17 violate energy conservation (i.e. the largest Lambert parameter, μ, that satisfies energy conservation is π^{-1} or about -5 dB[6]). However, this criterion is for the bistatic version of the model, and as Jackson and Richardson state, larger values are possible if backscatter enhancement is present. Figs. 15 demonstrates that backscatter enhancement is present for the largest roughness case, and therefore energy conservation is not violated by large values of μ or μ_p.

For scenarios with smaller kh, the fit to Lambert's law is not exact. The generalized Lambert law was fit to all the Dirichlet simulations with a fixed $L/\lambda = 100$. These results are shown in Fig. 17. For large values of the spectral strength, the fits show $p \approx 2$, which indicates a good fit to Lambert's law. Smaller spectral strengths show values of p between 2 and 4, with the upper limit indicating the shape of lowest-order PT and SSA(2) at small grazing angles. These empirical model fits are another way of showing a gradal departure from the SSA(2) or PT model shape at low grazing angles towards Lambert's law as kh is increased. Linear least squares was used to fit the model to the data by using $10 \log_{10} \sin\theta$ as the independent variable. The R^2 value of this linear fit was greater than 0.9 for all but two $\gamma = 3$ cases with the largest spectral strengths.

VII. CONCLUSION

The small slope approximation was compared to a benchmark integral equation solution for a power-law roughness spectrum, backscattering geometry, and various boundary conditions. The largest value of the parameters kh and s for which the SSA satisfied validity criteria were found. This research is a first step towards finding practical limitations of scattering models that are used to compare to real measurements of scattering from rough surfaces, whether from acoustic systems measuring the sea floor, or radar systems from natural terrain. A fruitful area of future work would be to perform a similar study for 2D roughness and a 3D acoustic medium, which would be more directly comparable to experiments[84]. However, fast methods for solving the required integral equations would need to be used.

ACKNOWLEDGMENTS

This work was funded by grant by the Office of Naval Research, for which the author is grateful. Numerical simulations were performed using the Hamming high performance computing system at the Naval Postgraduate School (NPS). Discussions with Dr. Sumedh Joshi regarding scattering models for rough surfaces and integral equation methods were a valuable part of the genesis and motivation of this work. This paper is dedicated to his memory. The opinions and views expressed are those of the author alone and do not necessarily represent those of the U.S. Government, U.S. Department of War or its

components, to include the Department of the Navy or the Naval Postgraduate School.

DATA AVAILABILITY

The simulations used for this work are available upon reasonable request to the author.

CONFLICT OF INTEREST

The author has no conflicts of interest to declare.

APPENDIX: PERTURBATION SERIES

The perturbation series for T is given by the sum

$$\begin{aligned} T \approx & A_0(k_{ix})\delta(k_{sx}-k_{ix})+ \\ & A_1(k_{sx},k_{ix})F(k_{sx}-k_{ix})+ \\ & \frac{1}{2}\int \mathrm{d}k_{1x} A_2(k_{sx},k_{ix},k_{1x})F(k_{sx}-k_{1x})F(k_{1x}-k_{ix}) \\ & +\ldots \end{aligned} \tag{A1}$$

The factors A_n can be calculated using the formula in Appendix K of Jackson and Richardson[6]. Using these formulas, the coefficients are

$$A_0(k_{ix}) = Q(k_{ix},k_{ix}) \tag{A2}$$

$$\begin{aligned} A_1(k_{sx},k_{ix}) = & -ik\left[\beta_0(k_{ix})Q(k_{sx},k_{ix})\right. \\ & \left. +M(k_{sx},k_{ix}E(k_{ix})Q(k_{ix},k_{ix}))\right] \end{aligned} \tag{A3}$$

$$\begin{aligned} A_2(k_{sx},k_{ix},k_{1x}) = & (-ik\beta_0(k_{ix}))^2 Q(k_{sx},k_{ix}) \\ & -(ik)^2 M(k_{sx},k_{ix})E^2(k_{ix})Q(k_{ix},k_{ix}) \\ & -2ikM(k_{sx},k_{sx}-k_{1x})E(k_{sx}-k_{1x}) \\ & \times A_1(k_{sx}-k_{1x},k_{ix}) \end{aligned} \tag{A4}$$

Note that the equation for A_1 has corrected a sign error appearing in Eq. (K43) of Jackson and Richardson[6]. The small slope approximation requires that $\Phi_1(k_{sx},k_{ix},0) = 0$, which in turn requires a symmetrized version of A_2. This version is denoted $\tilde{A}_2$, and the process by which this term is found is detailed in Berman[16]. The result of this manipulation is

$$\begin{aligned} \tilde{A}_2(k_{sx},k_{ix},k_{1x}) = & (-ik\beta_0(k_{ix}))^2 Q(k_{sx},k_{ix}) \\ & -(ik)^2 M(k_{sx},k_{ix})E^2(k_{ix})Q(k_{ix},k_{ix}) \\ & -ik\left[M(k_{sx},k_{sx}-k_{1x})E(k_{sx}-k_{1x})A_1(k_{sx}-k_{1x},k_{ix})\right. \\ & \left. +M(k_{sx},k_{ix}+k_{1x})E(k_{ix}+k_{1x})A_1(k_{ix}+k_{1x},k_{ix})\right] \end{aligned} \tag{A5}$$

The quantities Q, E, and M are reproduced here from Appendix K in Jackson and Richardson[6]. In terms of generic horizontal wave-number k_{1x} and k_{2x}, these quantities are

$$M(k_{1x},k_{2x}) = D^{-1}(,k_{1x})D(k_{1x},k_{2x}) \tag{A6}$$

$$Q(k_{1x},k_{2x}) = D^{-1}(k_{1x},k_{1x})S(k_{1x},k_{2x}) \tag{A7}$$

$$D(k_{1x},k_{2x}) = \begin{bmatrix} -1 & 1 \\ a_\rho B_0(k_{1x},k_{2x}) & B_1(k_{1x},k_{2x}) \end{bmatrix} \tag{A8}$$

$$S(k_{1x},k_{2x}) = \begin{bmatrix} 1 \\ a_\rho B_0(k_{1x},k_{2x}) \end{bmatrix}, \tag{A9}$$

where the function B_α is

$$B_\alpha(k_{1x},k_{2x}) = \frac{1-k_{1x}k_{2x}/k_\alpha^2}{a_\alpha \beta_\alpha(k_{2x})}. \tag{A10}$$

The diagonal matrix $E(k_x)$ is

$$E(k_x) = \begin{bmatrix} \beta_0(k_x) & 0 \\ 0 & -\beta_1(k_x)/a_1 \end{bmatrix}. \tag{A11}$$

The definition of D in Eq. (A8) corrects an error in Jackson and Richardson[6] reported in the list of errata.

CONFLICT OF INTEREST

The authors have no conflicts of interest to disclose.

DATA AVAILABILITY

The data that support the findings in this study are available from the corresponding author upon reasonable request.

[1] R. J. Urick, *Principles of Underwater Sound*, 3rd ed. (Peninsula, Los Altol Hills, California, 1983).

[2] D. A. Abraham, *Underwater Acoustic Signal Processing* (Springer International Publishing, 2019).

[3] M. Ainslie, *Principles of Sonar Performance Modelling* (Springer Berlin Heidelberg, 2010).

[4] L. Fonseca and L. Mayer, "Remote estimation of surficial seafloor properties through the application angular range analysis to multibeam sonar data," Marine Geophysical Researches **28**(2), 119–126 (2007) doi: mu10.1007/s11001-007-9019-4.

[5] C. Heinrich, P. Feldens, and K. Schwarzer, "Highly dynamic biological seabed alterations revealed by side scan sonar tracking of lanice conchilega beds offshore the island of sylt (german bight)," Geo-Marine Letters **37**(3), 289–303 (2016) doi: mu10.1007/s00367-016-0477-z.

[6] D. R. Jackson and M. D. Richardson, *High-Frequency Seafloor Acoustics* (Springer, New York, NY, 2007).

[7] E. Y. T. Kuo, "Wave scattering and transmission at irregular surfaces," The Journal of the Acoustical Society of America **36**(11), 2135–2142 (1964) doi: mu10.1121/1.1919334.

[8] E. Y. Harper and F. M. Labianca, "Perturbation theory for scattering of sound from a point source by a moving rough surface in the presence of refraction," J. Acoust. Soc. America **57**(5), 1044–1051 (1975) doi: mu10.1121/1.380572.

[9] E. Y. Harper and F. M. Labianca, "Scattering of sound from a point source by a rough surface progressing over an isovelocity ocean," The Journal of the Acoustical Society of America **58**(2), 349–364 (1975) doi: mu10.1121/1.380679.

[10] E. I. Thorsos and D. R. Jackson, "The validity of the perturbation approximation for rough surface scattering using a Gaussian roughness spectrum," J. Acoust. Soc. America **86**, 261–277 (1989).

[11] C. Eckart, "The scattering of sound from the sea surface," J. Acoust. Soc. America **25**, 566–570 (1953).

[12] D. R. Jackson, D. P. Winebrenner, and A. Ishimaru, "Application of the composite roughness model to high-frequency bottom backscattering," J. Acoust. Soc. America **79**, 1410–1422 (1986).

[13] A. G. Voronovich, "Tangent plane approximation and some of its generalizaztions," Acoustical Physics **53**, 298 – 304 (2007).

[14] A. G. Voronovich, "Small-slope approximation in wave scattering by rough surfaces," Sov. Phys. JETP **62**, 65–70 (1985).

[15] D. H. Berman and D. K. Dacol, "Manifestly reciprocal scattering amplitudes for rough interface scattering," J. Acoust. Soc. America **87**, 2024–2032 (1990).

[16] D. H. Berman, "Simulations of rough interface scattering," J. Acoust. Soc. America **89**(2), 623–636 (1991) doi: mu10.1121/1.400387.

[17] T. Yang and S. L. Broschat, "Acoustic scattering from a fluid–elastic-solid interface using the small slope approximation," The Journal of the Acoustical Society of America **96**(3), 1796–1804 (1994) doi: mu10.1121/1.410258.

[18] S. T. McDaniel and A. D. Gorman, "An examination of the composite-roughness scattering model," J. Acoust. Soc. America **73**, 1476–1486 (1983).

[19] G. Xu, B. T. Hefner, D. R. Jackson, A. N. Ivakin, and G. Wendelboe, "A physics-based inversion of multibeam sonar data for seafloor characterization," IEEE Journal of Oceanic Engineering **50**(2), 1325–1343 (2025) doi: mu10.1109/joe.2024.3467308.

[20] The composite roughness approximation has found application in modeling higher order moments of the scattered intensity[51,85–87].

[21] E. I. Thorsos, "The validity of the Kirchhoff approximation for rough surface scattering using a Gaussian roughness spectrum," J. Acoust. Soc. America **83**, 78–92 (1988).

[22] F. Fois, P. Hoogeboom, F. Le Chevalier, and A. Stoffelen, "Future ocean scatterometry: On the use of cross-polar scattering to observe very high winds," IEEE Transactions on Geoscience and Remote Sensing **53**(9), 5009–5020 (2015) doi: mu10.1109/tgrs.2015.2416203.

[23] P.-B. Wei, M. Zhang, R.-Q. Sun, and X.-F. Yuan, "Scattering studies for two-dimensional exponential correlation textured rough surfaces using small-slope approximation method," IEEE Transactions on Geoscience and Remote Sensing **52**(9), 5364–5373 (2014) doi: mu10.1109/tgrs.2013.2288278.

[24] V. Irisov, "Small slope approximation for microwave polarimetric observation of the sea surface," in *Proceedings of IGARSS '94 - 1994 IEEE International Geoscience and Remote Sensing Symposium*, IEEE (1994), Vol. 4 of *IGARSS-94*, pp. 2421–2423, doi: mu10.1109/igarss.1994.399757.

[25] R.-Q. Sun, M. Zhang, C. Wang, and Y. Chen, "Study of electromagnetic scattering from ship wakes on PEC sea surfaces by the small-slope approximation theory," Progress In Electromagnetics Research **129**, 387–404 (2012) doi: mu10.2528/pier12041405.

[26] I. Young and M. Donelan, "On the determination of global ocean wind and wave climate from satellite observations," Remote Sensing of Environment **215**, 228–241 (2018) doi: mu10.1016/j.rse.2018.06.006.

[27] I. G. Rizaev, O. Karakuş, S. J. Hogan, and A. Achim, "Modeling and sar imaging of the sea surface: A review of the state-of-the-art with simulations," ISPRS Journal of Photogrammetry and Remote Sensing **187**, 120–140 (2022) doi: mu10.1016/j.isprsjprs.2022.02.017.

[28] W. J. Plant, "A stochastic, multiscale model of microwave backscatter from the ocean," Journal of Geophysical Research: Oceans **107**(C9) (2002) doi: mu10.1029/2001jc000909.

[29] J. Johnson and M. Zhang, "Theoretical study of the small slope approximation for ocean polarimetric thermal emission," IEEE Transactions on Geoscience and Remote Sensing **37**(5), 2305–2316 (1999) doi: mu10.1109/36.789627.

[30] D. Hauser, S. Abdalla, F. Ardhuin, J.-R. Bidlot, M. Bourassa, D. Cotton, C. Gommenginger, H. Evers-King, H. Johnsen, J. Knaff, S. Lavender, A. Mouche, N. Reul, C. Sampson, E. C. Steele, and A. Stoffelen, "Satellite remote sensing of surface winds, waves, and currents: Where are we now?," Surveys in Geophysics **44**(5), 1357–1446 (2023) doi: mu10.1007/s10712-023-09771-2.

[31] P. A. Hwang, "Foam and roughness effects on passive microwave remote sensing of the ocean," IEEE Transactions on Geoscience and Remote Sensing **50**(8), 2978–2985 (2012) doi: mu10.1109/tgrs.2011.2177666.

[32] D. Horton, J. T. Johnson, M. Al-Khaldi, J. Park, and R. Bindlish, "A study of the second order small slope approximation for l-band backscattering from soil surfaces," in *IGARSS 2024 - 2024 IEEE International Geoscience and Remote Sensing Symposium*, IEEE (2024), pp. 4354–4357, doi: mu10.1109/igarss53475.2024.10642505.

[33] J. Hare, A. P. Lyons, and G. R. Venegas, "Measurements of the angular dependence of acoustic seafloor scattering in sandy sites," The Journal of the Acoustical Society of America **158**(3), 2225–2237 (2025) doi: mu10.1121/10.0039373.

[34] E. I. Thorsos, "Acoustic scattering from a "Pierson-Moskowitz" sea surface," J. Acoust. Soc. America **88**(1), 335–349 (1990) doi: mu10.1121/1.399909.

[35] S. L. Broschat and E. I. Thorsos, "An investigation of the small slope approximation for scattering from rough surfaces. Part II. numerical studies," J. Acoust. Soc. America **101**, 2615 – 2625 (1997).

[36] Y. Wang and S. L. Broschat, "A systematic study of the lowest order small slope approximation for a pierson–moskowitz spectrum," IEEE Geoscience and Remote Sensing Letters **8**(1), 158–162 (2011) doi: mu10.1109/lgrs.2010.2053193.

[37] J. A. Goff and T. H. Jordan, "Stochastic modeling of seafloor morphology: Inversion of Sea Beam data for second-order statistics," J. Geophys. Res. **93**, 13589 – 13608 (1988).

[38] K. Briggs, "Microtopographical roughness of shallow-water continental shelves," J. Oceanic Eng. **14**(4), 360 –367 (1989) doi: mu10.1109/48.35986.

[39] D. R. Jackson and K. B. Briggs, "High-frequency bottom backscattering: Roughness versus sediment volume scattering," J. Acoust. Soc. America **92**, 962–977 (1992).

[40] R. E. Kleinman and P. A. Martin, "On single integral equations for the transmission problem of acoustics," SIAM Journal on Applied Mathematics **48**(2), 307–325 (1988) doi: mu10.1137/0148016.

[41] R. F. Gragg, D. Wurmser, and R. C. Gauss, "Small-slope scattering from rough elastic ocean floors: General theory and computational algorithm," The Journal of the Acoustical Society of America **110**(6), 2878–2901 (2001) doi: mu10.1121/1.1412444.

[42] R. J. Soukup and R. F. Gragg, "Backscatter from a limestone seafloor at 2-3.4 kHz: Measurements and modeling," J. Acoust. Soc. America **113**, 2501–2514 (2003).

[43] D. R. Jackson, "High-frequency bistatic scatteirng model for elastic seafloors," TM 2-00, Applied Physics Laboratory, University of Washington Technical Memorandum (2000).

[44] D. R. Olson, A. P. Lyons, and T. O. Sæbø, "Measurements of high-frequency acoustic scattering from glacially eroded rock outcrops," J. Acoust. Soc. America **139**(4), 1833–1847 (2016) doi: mu10.1121/1.4945589.

[45] L. Greengard and V. Rokhlin, "A fast algorithm for particle simulations," Journal of Computational Physics **73**(2), 325–348 (1987) doi: mu10.1016/0021-9991(87)90140-9.

[46] N. A. Gumerov and R. Duraiswami, "A broadband fast multipole accelerated boundary element method for the three dimensional helmholtz equation," The Journal of the Acoustical Society of America **125**(1), 191–205 (2009) doi: mu10.1121/1.3021297.

[47] C. W. Holland and P. Neumann, "Sub-bottom scattering: A modeling approach," J. Acoust. Soc. America **104**(3), 1363–1373

(1998) doi: mu10.1121/1.424345.

[48]D. R. Jackson and A. N. Ivakin, “Scattering from elastic sea beds: First-order theory,” J. Acoust. Soc. America **103**, 336 – 345 (1998).

[49]D. Jackson and D. R. Olson, “The small-slope approximation for layered, fluid seafloors,” The Journal of the Acoustical Society of America **147**(1), 56–73 (2020) muhttps://doi.org/10.1121/10.0000470 doi: mu10.1121/10.0000470.

[50]C. W. Holland, S. Pinson, C. M. Smith, P. C. Hines, D. R. Olson, S. E. Dosso, and J. Dettmer, “Seabed structure inferences from TREX13 reflection measurements,” IEEE Journal of Oceanic Engineering **42**(2), 268–288 (2017) doi: mu10.1109/joe.2017.2658418.

[51]D. R. Olson and A. P. Lyons, “Resolution dependence of rough surface scattering using a power law roughness spectrum,” The Journal of the Acoustical Society of America **149**(1), 28–48 (2021) doi: mu10.1121/10.0002974.

[52]J. A. Goff, A. H. Reed, G. Gawarkiewicz, P. S. Wilson, and D. P. Knobles, “Stratigraphic analysis of a sediment pond within the new england mud patch: New constraints from high-resolution chirp acoustic reflection data,” Marine Geology **412**, 81–94 (2019) doi: mu10.1016/j.margeo.2019.03.010.

[53]A. Yaglom, *An Introduction to the Theory of Stationary Random Functions* (Prentice Hall, Englewood Cliffs, NJ, 1962).

[54]S. Rytov, I. Kravtsov, and V. Tatarskii, *Principles of Statistical Radiophysics 3: Elements of random fields* (Springer-Verlag, Berlin, 1989).

[55]A. Khintchine, “Korrelationstheorie der stationären stochastischen prozesse,” Mathematische Annalen **109**(1), 604–615 (1934) doi: mu10.1007/bf01449156.

[56]A. G. Voronovich, *Wave Scattering from Rough Surfaces*, second ed. (Springer, Berlin Heidelberg, 1999).

[57]E. I. Thorsos and S. L. Broschat, “An investigation of the small slope approximation for scattering from rough surfaces. Part I. theory,” J. Acoust. Soc. America **97**, 2082 – 2093 (1995).

[58]A. D. Pierce, *Acoustics: An introduction to its physical principles and applications* (the Acoustical Society of America, 1994).

[59]O. Steinbach, *Numerical Approximation Methods for Elliptic Boundary Value Problems* (Springer, New York, NY, 2008).

[60]D. R. Olson and D. Jackson, “Scattering from layered seafloors: Comparisons between theory and integral equations,” The Journal of the Acoustical Society of America **148**(4), 2086–2095 (2020) doi: mu10.1121/10.0002164.

[61]T. W. Wu, ed., *Boundary Element Acoustics: Fundamentals and Computer Codes* (WIT Press, Southampton, UK, 2000).

[62]M. J. Isakson and N. P. Chotiros, “Finite element modeling of acoustic scattering from fluid and elastic rough interfaces,” IEEE Journal of Oceanic Engineering **40**(2), 475–484 (2015) doi: mu10.1109/joe.2014.2313060.

[63]F. N. Fritsch and J. Butland, “A method for constructing local monotone piecewise cubic interpolants,” SIAM Journal on Scientific and Statistical Computing **5**(2), 300–304 (1984) doi: mu10.1137/0905021.

[64]D. E. Amos, “Algorithm 644: A portable package for Bessel functions of a complex argument and nonnegative order,” ACM Transactions on Mathematical Software **12**(3), 265–273 (1986) doi: mu10.1145/7921.214331.

[65]B. Kernighan and D. Ritchie, *The C Programming Language*, 2nd ed. (Prentice Hall, 1988), muhttps://books.google.com/books?id=FGkPBQAAQBAJ.

[66]J. Neyman and E. S. Pearson, “The testing of statistical hypotheses in relation to probabilities a priori,” Mathematical Proceedings of the Cambridge Philosophical Society **29**(4), 492–510 (1933) doi: mu10.1017/s030500410001152x.

[67]O. I. Yordanov and K. Ivanova, “Kirchhoff diffractals,” Journal of Physics A: Mathematical and General **27**(17), 5979 (1994).

[68]D. M. Drumheller and R. F. Gragg, “Evaluation of a fundamental integral in rough-surface scattering theory,” J. Acoust. Soc. America **110**(5), 2270–2275 (2001) doi: mu10.1121/1.1412445.

[69]D. R. Jackson, D. P. Winebrenenr, and A. Ishimaru, “Comparison of perturbation theories for rough-surface scattering,” J. Acoust. Soc. America **83**, 961 – 969 (1988).

[70]E. G. Liszka and J. J. McCoy, “Scattering at a rough boundary - extensions of the kirchhoff approximation,” J. Acoust. Soc. America **71**, 1093–1100 (1982).

[71]A. G. Voronovich, “Non-local small-slope approximation for wave scattering from rough surfaces,” Waves in Random Media **6**(2), 151–167 (1996) doi: mu10.1088/0959-7174/6/2/005.

[72]E. I. Thorsos and D. R. Jackson, “Studies of scattering theory using numerical methods,” Waves Random Media **1**(3), S165–S190 (1991) doi: mu10.1088/0959-7174/1/3/014.

[73]J. S. Chen and A. Ishimaru, “Numerical simulation of the second-order kirchhoff approximation from very rough surfaces and a study of backscattering enhancement,” J. Acoust. Soc. America **88**, 1846–1850 (1990).

[74]A. G. Voronovich, “A two-scale model from the point of view of the small-slope approximation,” Waves Rand. Media **6**(1), 73–83 (1996) doi: mu10.1088/13616679609409796.

[75]J. H. Lambert, *Photometria sive de mensure de gratibus luminis, colorum umbrae* (Eberhardi Klett, 1760).

[76]Subsequent research has shown the original Lambert model to be insufficient (e.g. see Hapke[88] and references therein).

[77]E. Kunz and R. Gauss, “Bottom backscattering strengths measured at 2-5 kHz in shallow water west of scotland,” in *Proceedings of OCEANS 2005 MTS/IEEE*, IEEE (2005), doi: mu10.1109/oceans.2005.1640008.

[78]R. J. Urick, “The backscattering of sound from a harbor bottom,” J. Acoust. Soc. America **26**, 231–235 (1954).

[79]C. M. McKinney and C. D. Anderson, “Measurements of backscattering of sound from the ocean bottom,” J. Acoust. Soc. America **36**, 158–163 (1964).

[80]M. B. Fairbairn, “Planetary photometry: The Lommel-Seeliger law,” Proc. Roy. Astr. Soc. Can. **99**(3), 92–93 (1999).

[81]P. M. Ogden and F. T. Erskine, “Surface scattering measurements using broadband explosive charges in the critical sea test experiments,” The Journal of the Acoustical Society of America **95**(2), 746–761 (1994) doi: mu10.1121/1.408385.

[82]J. A. Gruber and D. R. Olson, “Scattering measurements of rocky seafloors using a split-beam echosounder,” JASA Express Letters **4**(2) (2024) doi: mu10.1121/10.0024755.

[83]R. P. Chapman and J. H. Harris, “Surface backscattering strengths measured with explosive sound sources,” The Journal of the Acoustical Society of America **34**(10), 1592–1597 (1962) doi: mu10.1121/1.1909057.

[84]S. M. Joshi, “Quantifying three dimensional effects in acoustic rough surface scattering,” Master’s thesis, The University of Texas at Austin (2011).

[85]L. Hellequin, J. M. Boucher, and X. Lurton, “Processing of high-frequency multibeam echo sounder data for seafloor characterization,” IEEE J. Oceanic En **28**(1), 78–89 (2003) doi: mu10.1109/JOE.2002.808205.

[86]G. Le Chenadec, J.-M. Boucher, and X. Lurton, “Angular dependence of K-distributed sonar data,” IEEE Trans. Geosci. Rem. Sens. **45**(5), 1224–1235 (2007) doi: mu10.1109/TGRS.2006.888454.

[87]A. P. Lyons, D. R. Olson, and R. E. Hansen, “Modeling the effect of random roughness on synthetic aperture sonar image statistics,” The Journal of the Acoustical Society of America **152**(3), 1363–1374 (2022) doi: mu10.1121/10.0013837.

[88]B. Hapke, “Bidirectional reflectance spectroscopy: 1. theory,” Journal of Geophysical Research: Solid Earth **86**(B4), 3039–3054 (1981) doi: mu10.1029/jb086ib04p03039.